

Model catalysts based on Au clusters and nano particles

Niklas Nilius, Thomas Risse, Shamil Shaikhutdinov, Martin Sterrer, Hans-Joachim Freund*

**Fritz Haber Institut of the Max Planck Society,
Department of Chemical Physics, Faradayweg 4-6, 14195 Berlin, Germany*

Abstract Small Au particles have been shown to exhibit interesting catalytic properties. In an attempt to parallel catalytic studies on powder supports we have undertaken a series of model studies using oxide films as support. We address the formation of Au aggregates as a function of size starting from Au atoms to clusters and islands of larger size, and as a function of the support. In addition we have studied different support materials such as alumina and iron oxide and we compare ultrathin and thicker oxide films of the same material (MgO). From a comparison of charge transfer through ultrathin films with the situation encountered in thicker films, we propose the use of dopants in bulk materials to control particle shape. We include the study of carbon monoxide adsorption on Au clusters of varying size. It is demonstrated how chemical modification (hydroxylation) of oxide supports influence particle growth and properties. Finally, we report on effects to study the processes involved in particle growth by wet impregnation in order to bridge the gap to catalyst preparation under realistic conditions. On that basis one may now compare properties of supported particles prepared in ultrahigh vacuum using physical vapor deposition with those prepared by wet impregnation.

Keywords Au clusters, oxide films, electronic properties, dopants, adsorption, chemical modification, wet impregnation

1 Introduction

In 1984 Michael Mingos published two papers important for the present review [1,2]. One paper published in *Account of Chemical Research* in which he summarized the state of affairs concerning the prediction of structures of cluster compounds based on their total number of valence electrons. He and Ken Wade pioneered in the early 70s [3] what has been called the Polyhedral Skeletal Electron Pair Theory, an extension of the VSEPR (valence shell electron pair repulsion theory) [4] of molecular compounds. This led then to setting up of electron counting rules, which connect the number of available valence electrons with stability

criteria for particular cluster geometries. The second paper was published in Gold Bulletin entitled "Gold cluster compounds: are they metals in miniature?". The results of his thoughts about surface-clusters analogies may be summarized with two quotes from his paper: "The writer's personal view is that such analogies bear the same deficiencies as attempting to relate benzene to graphite and strained hydrocarbons such as cubane, C₈H₈, to diamond." and "These results suggest that those scientists studying the catalytic properties of crystallites of gold on inert supports should recognize that the clusters may change their geometries as a result of introducing substrates and changes in environment." The latter, in particular, is an important observation that many researchers in catalysis, even today, have not taken into consideration, seriously. It is one of the messages that this paper wants to convey: the flexibility of nano particles to respond to the environment, for example the support, is the source for their reactivity. By controlling the environment and using the flexibility of nano particles one may change not only morphologies and structures but also charge states of active components. For the latter, the metal-oxide interface plays an important role and thus cannot be taken into consideration by the single crystal approach, so successful in the past, culminating in the 2007 Nobel Prize for Gerhard Ertl. [5] While solid state theory has provided fundamental insights into processes and intermediates on single crystal surfaces using density functional calculations with periodic boundaries these approaches have to be substantially modified to allow for successful treatment of nano particles of relevant size on an oxide support. In this respect, also, calculations on free clusters may only be used for reference purpose. Our group has pointed this out in a number of reviews on modeling heterogeneous catalysts. [6-9] The present review goes somewhat beyond previous ones, as we attempt to make contact between model systems of various degrees of sophistication and the preparation of the same model systems via wet impregnation techniques. We have chosen Au supported on simple, non-reducible oxides as the example, as Au shows a pronounced catalytic activity when it exhibits nanoparticulate morphology and is in interaction with a support so beautifully pointed out in the late 1980ies by Masatake Haruta [10,11].

The chapter is organized as follows:

After a short introduction into our philosophy for preparing model systems of supported dispersed metal catalysts, we proceed by showing how one may build up Au particles from the individual atom to intermediate sized Au clusters towards nano particles of a few nanometers in size. We will then proceed to larger islands and address the question how one may be able to learn about the convergence of cluster size towards representation of a fully developed metal. As we are working with thin oxide films as supports in order to be able to use charged (entities) particles as information carriers we also address the question of film thickness to represent the bulk situation. In fact, out of this approach, the interesting observation of the influence of dopants in the support arose and this problem will be addressed as well. A brief intermezzo on CO adsorption will also be included. As a first step towards the study of particle preparation via wet chemical techniques we have

studied substrate modification, basically by hydroxylation, and its influence on the electronic and structural properties of metal deposits. Finally, we compare properties of deposits prepared via wet impregnation on oxides with systems prepared by physical vapor deposition on oxides using ultra-high vacuum (UHV) based techniques, and at the end conclusions within a synopsis will be presented.

2 Binding of Single Metal Atoms and Small Clusters to Oxide Surfaces

2.1 General Considerations.

Adsorption on defect-free oxides is generally weak given the high degree of bond saturation at their surface and the large gap that governs their electronic structure [12-18]. Metal atoms deposited onto pristine oxides have essentially two means to interact with the surface. The first one, being accessible to all atoms, arises from van der Waals or dispersive forces, i.e. the ad-atom gets polarized in the Madelung field of the oxide and experiences dipolar coupling to the surface. Depending on the atom polarizability, the resulting adsorption energies are of the order of 0.5 eV or below for a single atom. The second interaction channel that is relevant for open-shell *d* and *f*-elements is direct hybridization between orbitals of the ad-species and the oxide surface. Especially the overlap between the *d*-states of transition metal atoms and the *2p* orbitals of the surface oxygen plays an important role, and enables an increase in the metal-oxide bond strength to more than 1.0 eV [19-21]. Naturally, this channel is dominant for metals with partly filled *d*-shells (Cr, Mn, Fe) and loses influence for semi-noble and noble metals, e.g. Pt, Cu, Ag and Au.

Oxide materials are never perfect and therefore surface defects need to be considered as potential binding sites for metal atoms [22]. Oxide defects often give rise to considerable variations in the electrostatic potential, which originate from unbalanced charges and cannot be screened due to the low density of free carriers in the insulating material. In covalently-bound oxides, dangling bond states may emerge at the defect site, reflecting the rigid lattice structure of the system that does not support bond reorganization. Whereas dangling bond states are highly susceptible to form covalent bonds to metal ad-atoms, electrostatic forces and charge transfer processes become relevant in the presence of charged defects in ionic oxides. Oxygen vacancies in MgO, for example, are able to exchange electrons with metallic adsorbates, which enable strong Coulomb attraction between both partners. A model case for this scenario is the interaction between a doubly occupied O-defect (F^0 center) and a Au atom, in which the gold turns anionic and binds with more than 3.0 eV to the surface [23]. The opposite scenario, electron

flow into an electron trap in the oxide lattice (e.g. an F^{2+} center) is observed for electropositive ad-species and governs for instance the adsorption of alkali metals to different surfaces. Defect-mediated interaction schemes exceed the binding potential of the regular surface by up to a factor of three, underlining the significance of such lattice irregularities for the nucleation and growth of metals on oxide materials.

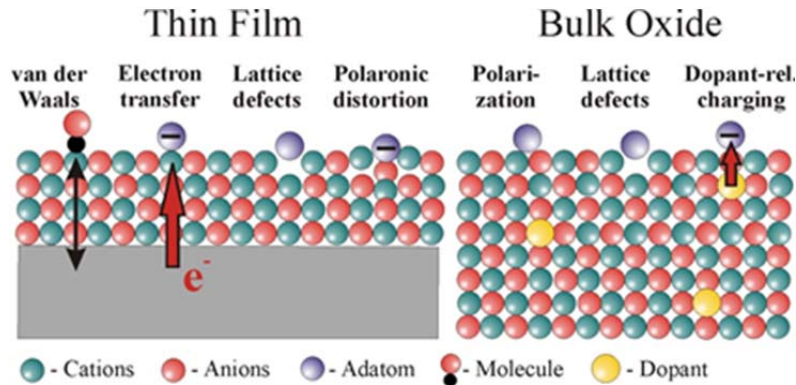


Figure 1: Different binding mechanisms of metal ad-atoms on thin films and bulk oxides.

A particularly interesting approach to modify the metal-oxide adhesion without generating surface defects is the insertion of charge sources directly into the oxide lattice (Figure 1). Two approaches have been proposed in the literature and were successfully realized in experiments. In a first scenario, the bulk oxide support is transformed into a thin film grown on a metal single crystal [24-26]. The metal substrate acts as infinite charge reservoir and on readily exchange electrons with ad-atoms bound to the surface of the thin film. A different electron potential in both subsystems is requirement for the charge transfer to occur, however this situation is often fulfilled as thin oxide films usually alter the work function of the pristine metal beneath [27]. In the second scenario, doping with aliovalent impurity ions may be exploited to introduce charges into the interior of thick films and even bulk oxides. Also in this case, charge transfer into the ad-species has been revealed, the direction of which is given by the nature of the dopant in conjunction with the electro-negativity of the adsorbate. Again, charge exchange is connected with a considerable increase of the metal-oxide adhesion. To give an estimate for the efficiency of charge-mediated interaction schemes, DFT calculations have revealed an increase in binding energy from 0.9 eV for neutral Au on defect-free MgO to 2.3 eV for Au^- species on thin MgO/Mo(001) films [28]. In the following, we will substantiate these general considerations with a number of experiments performed in our group. Whereas in the first part, the relevance of charge transfer for binding of single atoms to oxide surfaces is discussed, consequences on the growth and electronic properties of metal aggregates are in the focus of the later sections.

2.2 Role of charge transfer for binding single ad-atoms to oxide thin films.

A first hint for the formation of charged adsorbates on thin oxide films came from low-temperature scanning tunneling microscopy (STM) experiments performed on 3 ML MgO/ Ag(001) exposed to small amounts of Au [15]. Whereas on bulk oxides, gold shows a strong tendency for aggregation, mainly isolated atoms are detected on the thin film even at high gold exposure. Moreover, the ad-species self-assemble into a hexagonal superlattice on the film surface, with the Au-Au distance depending exclusively on the coverage and not on the MgO crystal structure (Figure 2A). This unexpected ordering effect provides first evidence for the charged nature of the Au atoms on MgO films, as equally-charged species tend to maximize their inter-atomic distance in order to reduce the mutual Coulomb repulsion. A similar phenomenon was found for alkali atoms on metal and semiconductor surfaces before and was assigned to a positive charging upon adsorption [29-31]. Conversely, the Au atoms on the MgO films charge up negatively, as their 6s orbital gets filled with electrons from the Ag(001) support below the oxide spacer layer. The charge exchange is enabled by the high electro-negativity of gold in combination with a small work function of the Ag-MgO system, both effects promoting an electron release towards ad-gold [27,28]. The experimentally deduced charging scenario was corroborated by DFT calculations that computed a Bader charge of $-1|e|$ at the Au atoms in addition to the expected increase in binding energy [32].

However, charge-mediated adsorption on oxide thin films is rather the exception than the rule, and requires a favorable electronic structure of the adsorbate. Counter examples are Pd atoms that, in contrast to Au atoms, do not possess a low-lying affinity level that can be filled with extra electrons from the MgO/Ag support. In fact, the Pd 5s, as the lowest unoccupied atomic orbital, is located well above the Fermi level of the thin-film system and therefore not accessible to electron transfer. As a result, the Pd atoms remain neutral upon adsorption and do not experience any self-ordering on the MgO surface (Figure 2B) [33]. Apart from their random distribution, the Pd atoms exhibit a high tendency to assemble into small aggregates even at low coverage, mimicking the anticipated binding behavior of metals on bulk oxides in absence of charge transfer.

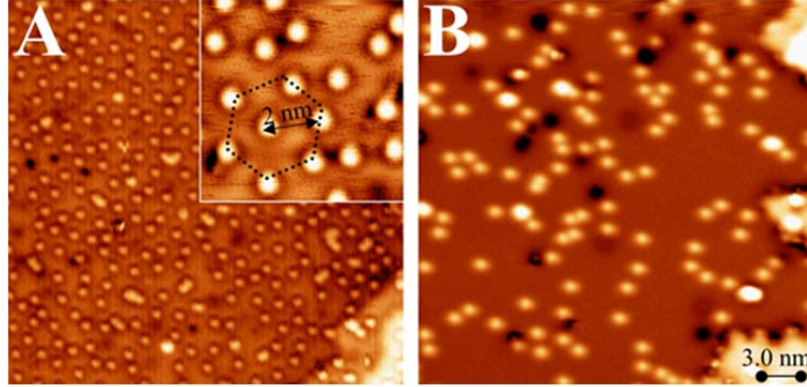


Figure 2: STM image of (A) single Au and (B) single Pd ad-atoms on a 3 ML thick MgO film grown on Ag(001) ($30 \times 30 \text{ nm}^2$). While the negatively charged Au atoms self-assemble into a hexagonal pattern (see inset), the neutral Pd atoms are randomly distributed on the oxide surface and show a large tendency to aggregate into clusters. A negative charge on the Au species is also compatible with a distinct sombrero-like shape observed in low-bias STM images. Black dots in both images are attributed to defects in the oxide film [32].

Charge-driven adsorption schemes were observed for many other thin-film systems, using not only metal ad-atoms but also molecular species [34,35]. Particularly interesting in this context are experiments on a 5 Å thick alumina film grown on NiAl(110) [36], as the results provide direct insight into the direction of the charge transfer and the number of exchanged electrons (Figure 3) [37]. Although charge transfer into the Au atoms prevails also in this case, the interaction involves a certain bond reorganization in the oxide and therefore deviates from the more simple MgO/Ag(001) case [32]. The Au atoms bind exclusively to Al³⁺ ions in the alumina surface, and no adsorption to anionic lattice sites is revealed (Figure 3A). Upon bond formation, the Al ion below the gold is lifted above the surface plane. This upward motion of the Al³⁺ leads to a homolytic rupture of the bond to the oxygen in the layer beneath. The Au atom takes up the electron donated by the Al ion, while the electron deficiency at the oxygen is balanced by back-bonding it to an Al atom in the NiAl(110) metal surface. The involvement of the metal substrate thus reinforces the interaction between ad-atom and surface, whereby not only charges are shuttled through the oxide, but the film reorganizes its internal bonding network in order to accommodate the gold. In numbers, a participation of the NiAl support leads to an increase of the Au-alumina adsorption strength from 1.0 to 2.1 eV, emphasizing once more the importance of charge transfer [37]. It should be added that the Au-induced bond cleavage in the alumina film can be considered as an extreme form of a polaronic lattice distortion, being a typical response of an ionic oxide to stabilize charged adsorbates on its surface [38].

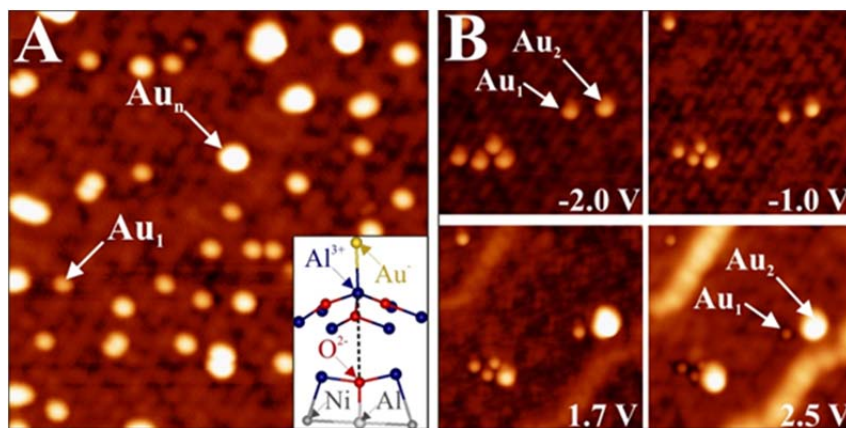


Figure 3: (A) STM image of Au monomers and small aggregates on alumina/NiAl(110) (-1.5 V, 18×18 nm²). The inset shows a ball-stick model of a monomer bound to an Al surface ion. (B) Image series, showing a small alumina region as a function of bias voltages (15×15 nm²). The various Au species undergo large contrast changes as a function of the imaging conditions [39].

The extra charges localized in alumina-bound Au atoms are responsible for a distinct contrast evolution in STM images taken as a function of sample bias (Figure 3B) [39]. At negative voltage (probing the occupied sample states), Au monomers are imaged as circular protrusions of ~ 6 Å diameter and ~ 1 Å apparent height. This height value decreases at positive polarity and finally reverses at 3.0 V, when the Au atoms show up as shallow depressions in the surface (Figure 4A). At intermediate voltages (between +2.0 and +3.0 V), the ad-species are surrounded by a characteristic sombrero ring, again being the typical fingerprint of charged adsorbates (Figure 3B and Figure 2a) [40,41]. According to the Tersoff-Hamann theory for vacuum tunneling, a negative contrast indicates a lower state density of the ad-atom as compared to the surrounding oxide, which forces the tip to approach the surface in order to maintain the preset tunnel current [42]. This decrease in state density is easily explained with a local upward bending of the oxide bands, in response to the negatively charged Au atom. Whereas tunneling is efficient in regions away from the Au-, as the oxide conduction band provides suitable final states, it remains blocked at the ad-atom site due to up-shift of the band onset at this location (Figure 4B, inset). Such upward bending is compatible with the accumulation of negative surface charges, exerting a repulsive interaction on the alumina electronic states [43], while positive charges would result in a downward bending of the bands and does not explain the experimental observations [44]. Assuming a screened Coulomb interaction:

$$V = -\frac{q}{4\pi\epsilon_0\epsilon_r r} \quad (1)$$

with an alumina dielectric constant of $\epsilon_r = 10$ and an Au excess charge of $q = -1|e|$, the upward bending calculates to $+1.8$ eV in distance $r = 1$ Å from the anion [43]. This value matches the bias window of 3.0-4.5 V, in which the Au atom appears with negative contrast in the STM images. The contrast reversal observed for Au atoms on alumina thin films therefore provides additional evidence for the charge-transfer that accompanies the interaction of gold with oxide thin films [28]. We note in passing that no contrast reversal is observed for Au dimers, which appear bright over the entire bias range (Figure 4B). The reason is the Au_2 electronic structure, which exhibits an intrinsic electronic state at 2.5 eV that compensates for the LDOS reduction due to band bending [39].

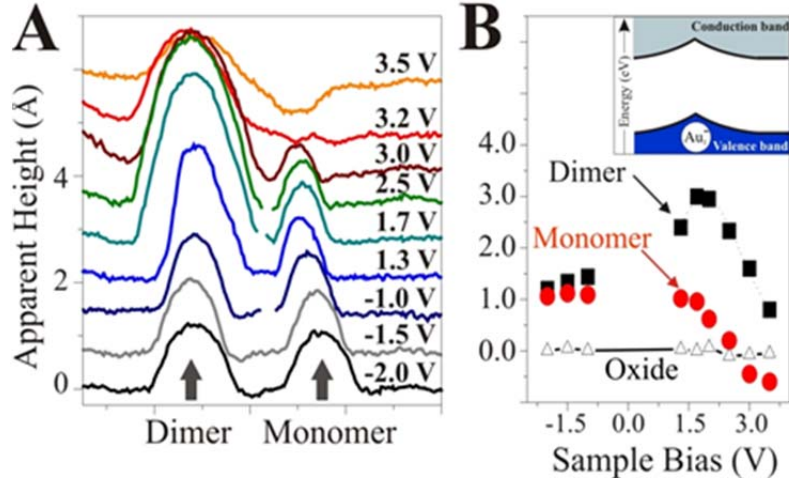


Figure 4: (A) Line profiles and (B) apparent heights of an Au monomer and dimer on alumina/NiAl(110) taken as a function of the bias voltages. The monomer turns into a depression above 3.0 V, as its negative charge triggers an upward bending of the alumina bands (see inset). The dimer appears bright due to tunneling through its LUMO located at 2.5 eV [37].

Charge transfer across oxide thin films does not necessarily lead to the formation of anionic gold species. In fact, the direction of charge transfer depends on the position of the Au affinity level (the Au 6s orbital) with respect to the Fermi level of the metal-oxide system. Because the level position of individual Au ad-atoms is largely governed by the vacuum energy, which is, in turn, given by the work function ϕ of the metal-oxide system, it is the latter quantity that determines the direction of the charge flow [38]. In general, low work function systems promote an electron flow into the gold, while the opposite trend is revealed for systems with high ϕ values. The two oxide films discussed so far, MgO/Ag and Alumina/NiAl

are characterized by a low work function, because the oxide layer prevents electron spillout from the metal surface and therewith removes a main reason for the high work function of non-alkali metals. A counter example is the FeO thin film that can be grown on Pt(111). Already the bare Pt(111) surface features an exceptionally high work function and this situation does not change upon FeO deposition. The reason is that the FeO film is of polar nature and features an intrinsic surface dipole with the negative side pointing towards the surface (oxygen termination) [45]. In this particular case, the Au atoms lose electrons to the film and become positively charged upon adsorption [46]. Although the direction of the charge flow is opposite to the one on magnesia and alumina, the resulting binding principles are similar and arise from a combination of electrostatic interactions and polaronic lattice distortion of the ionic oxide in presence of the charged ad-species.

2.3 Charge-mediated growth of metallic chains on oxide thin films.

The charge transfer that governs the binding of Au monomers to oxide thin films affects also the aggregation behavior of the gold at higher exposure. At cryogenic temperature, aggregation of equally charged ad-atoms is inhibited due to the Coulomb repulsion, giving rise to the formation of ordered ad-atom patterns as shown in Figure 2A. The repulsion is overcome, however, when dosing the gold at elevated temperature, e.g. 100 K. In this case, the Au atoms assemble into 1D atom chains at low coverage, as observed on both magnesia [47,48] and alumina films [40]. The smallest aggregate is a flat-lying dimer with 9 Å apparent lengths, while longer chains contain between three and seven atoms and are 12 to 22 Å long (Figure 5). The development of 1D chains on thin films is in contrast to the common behavior on bulk oxides, where 3D clusters are energetically favorable at any coverage due to the weak metal-oxide adhesion [26,49].

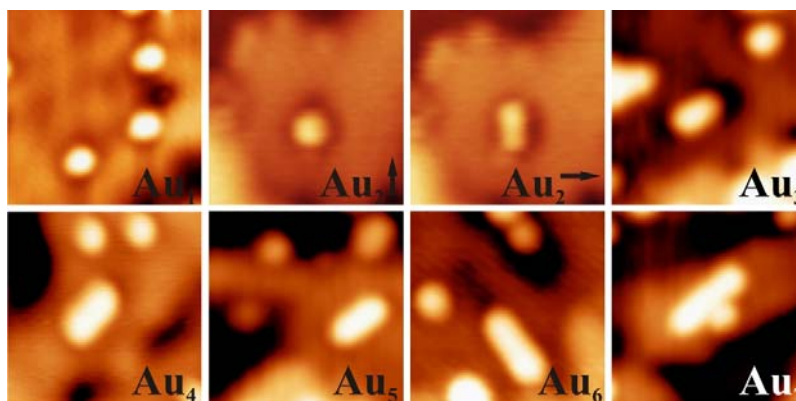


Figure 5: STM images of Au monomers, dimers and different chains on 2ML MgO/Ag(001) (-0.4 V, $19 \times 19 \text{ nm}^2$). For the dimer, an upright ($\text{Au}_2\uparrow$) and a flat-lying isomer is observed ($\text{Au}_2\rightarrow$) [48].

The development of Au atom-chains seems unexpected at first glance as the number of stabilizing Au-Au bonds is small with respect to 2D and 3D aggregates. However, the linear atom arrangement is in agreement with the charged nature of the aggregates. Similar to the monomer case, electron transfer through the oxide film into the Au cluster is active and increases the electrostatic coupling to the oxide lattice. Conversely, the charge transfer leads to a Coulomb repulsion in the aggregate that may be minimized when the extra electrons are separated over large distances. Minimization of Coulomb repulsion in electron-rich aggregates is therefore the fundamental reason for the development of 1D cluster shapes, and no 1D chains are expected in the absence of charge-transfer through the oxide films [47,48].

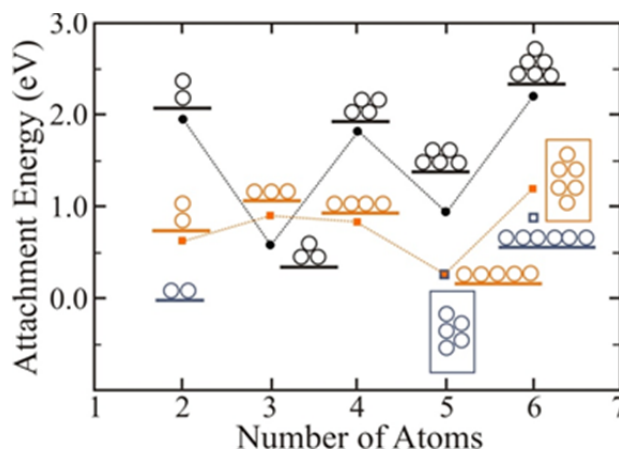


Figure 6: Attachment energies to form the displayed Au clusters, calculated for bulk MgO(001) (black circles) and 2ML MgO/Ag(001) films (orange squares). The blue squares depict the second most stable isomers on the thin film. On the oxide film, linear configurations are energetically preferred up to Au5, when planar isomers become more stable. The odd-even oscillations in the attachment energy are related to the high energy of open-shell systems containing an unpaired electron. They are less pronounced on thin MgO films due to the screening influence of the Ag support [48].

Also for Au aggregates bound to MgO/Ag(001) [47] and MgO/Mo(001) films [50], the concept of charge transfer has been verified by DFT calculations. Two configurations have been identified for the Au dimer, a neutral and upright one that binds to an O^{2-} ion in the MgO surface and a flat-lying, negatively charged species (Bader charge $-0.8|e|$) that bridges two Mg^{2+} or two hollow sites. The flat-lying configuration is thermodynamically preferred by 0.34 eV, a finding that explains its abundance in STM images of the MgO film (Figure 5) [47]. The prefer-

ence of charged over neutral Au clusters becomes even more pronounced for larger aggregates [48]. An Au_3^- chain for example (Bader charge $-1|e|$) has a higher binding energy than various neutral isomers (Figure 6). This finding holds for Au tetramers, where a doubly charged Au_4 chain (Bader value: $-1.6|e|$) is energetically preferred over different rhomboidal structures that can be found on bulk MgO(001). Note that the two extra electrons in the Au_4 chains are localized at the terminal atoms, emphasizing the shape-determining role of the Coulomb repulsion. With increasing atom count, 2D Au aggregates gain stability with respect to 1D configurations; as the formation of additional Au-Au bonds outweighs the energy surplus due to charge delocalization [48]. Whereas, a doubly negatively charged Au_5^{2-} chain is still iso-energetic with a flat-lying Au_5^- sheet on MgO/Ag(001), a 2D Au_6 island has already a lower energy than the corresponding linear structure (Figure 6). The critical atom number at which the 1D \rightarrow 2D dimensionality crossover occurs has been determined to five/six, both in experiment and theory.

So far, the amount of charge transfer into oxide-supported Au clusters has proven mainly by DFT calculations. However, this quantity can be accessed also by experiment, if the electron filling of specific quantum well states (QWS), in particular, of the highest-occupied (HOMO) and the lowest-unoccupied (LUMO) state can be measured with STM conductance spectroscopy. How this technique is exploited to quantify the charge transfer into Au chains on alumina thin films is demonstrated in the following (Figure 7) [37,40].

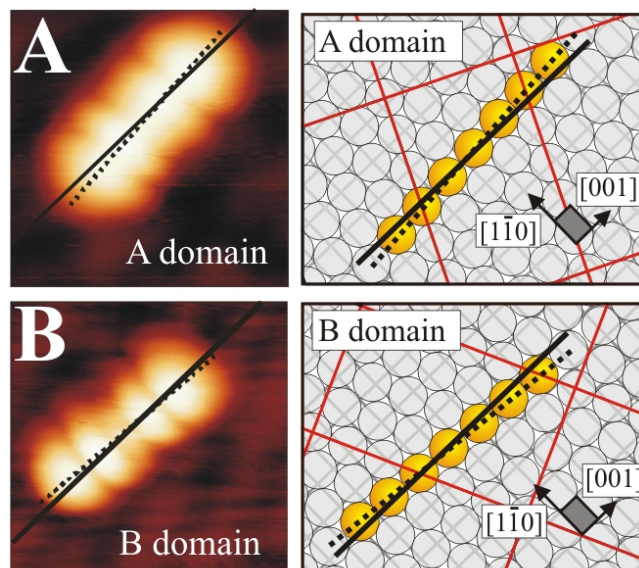


Figure 7: STM image and structure model for Au₇ chains bound to the two reflection domains in the alumina/NiAl(110) film (5 × 5 nm²). The chain orientation and the NiAl [001] direction are indicated by dashed and solid lines, respectively. Although the two domains are tilted against each other by 48°, the chains closely follow the NiAl [001] direction in both cases. The sketches on the right side show the Al₂³⁺ top layer (open spheres), the Au chain atoms (yellow, filled spheres), as well as the NiAl and alumina unit cells, being depicted with grey and red lines, respectively [40].

Also on alumina films, gold spontaneously forms linear clusters that are 8-22 Å long and contain between two and seven atoms [40,37]. These Au chains exhibit a particularly simple electronic structure that arises from the overlap of Au 6s and 6p orbitals to QWS formed in the 1D potential well [43,51]. There, the HOMO of the Au monomer derives from the Au 6s orbital and is doubly occupied ($E_{\text{bind}} = -1.3$ eV, Figure 8A). This double occupancy reflects the negative charge on the ad-atom, as gas phase Au features an Au 6s¹ ground state. The LUMO is a pz-like state that locates at +2.5 eV above EF hence inside the alumina conduction band. In Au dimers, the two 6s orbitals hybridize and form two new states at -0.3 eV and -1.5 eV. Both states are filled, which brings the total number of s-electrons in the dimer to four. As two of these electrons are transfer-electrons from the NiAl substrate, the Au₂ is twofold negatively charged. The Au₂ LUMO shifts to +1.9 eV due to the superposition of the two p_z states of each monomer (Figure 8B). In linear Au₃, a third s-like state appears directly at the Fermi level, while the two other QWS shift to -1.8 and -2.5 eV. Due to the half-filled nature of the HOMO, five s-electrons occupy the Au₃ valence orbitals, three intrinsic Au 6s electrons and two transfer-electrons from the metal beneath. The lowest unoccupied Au₃ states are the symmetric and anti-symmetric combination of the 6p_z orbitals, giving rise to two QWS at +1.9 and +2.8 eV, respectively.

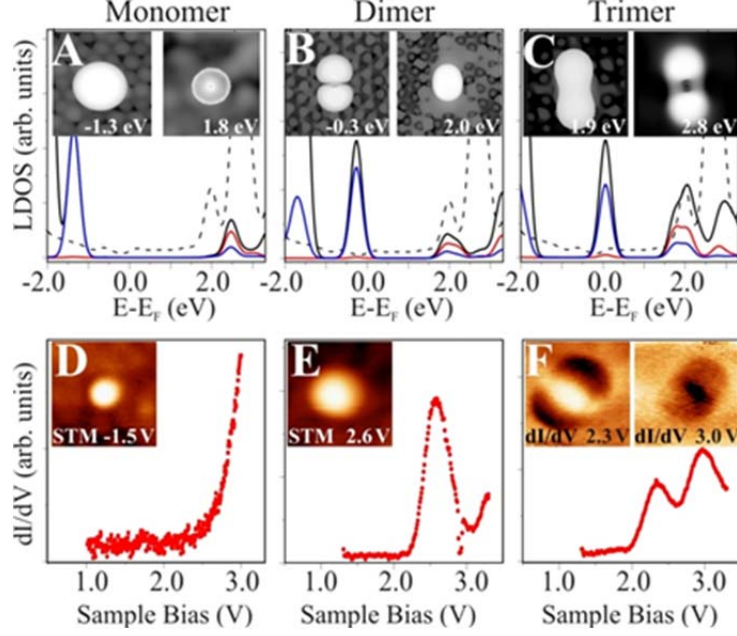


Figure 8: Spin-averaged LDOS and orbital shapes for (A) an Au monomer, (B) a dimer and (C) a trimer on alumina / NiAl(110), as calculated with DFT. The black line marks the total Au LDOS, the blue and red lines denote the s - and p_z -contributions, respectively. The dashed line depicts the alumina states. (D,E) Experimental dI/dV spectra and topographic images of an Au monomer and a dimer. (F) Trimer spectrum with dI/dV images taken at the two peak positions. All images are $4.5 \times 4.5 \text{ nm}^2$ in size; the set-point for spectroscopy was set to 3.0 V.

In extension of this concept, the electronic structure of a m -atom Au chain arises from the consecutive splitting of the $6s$ and $6p$ -like states and results in the development of m mainly occupied s -derived QWS and m empty states with p_z -character (Figure 9). The s -like states display the characteristic properties of a particle-in-a-box system with infinite walls [43]. The eigen-functions are sinusoidals ($\psi_n = \sin k_n x$), defined by a wave-number k_n that is proportional to the inverse box-length L and a quantum number n : ($k_n = n\pi/L$). The resulting electron distribution in the n th QWS (ψ_n^2) is given by n maxima separated by $n-1$ nodal planes along the chain axis, while the eigen-energies follow a parabolic dispersion relation:

$$E_n = E_0 + \frac{\hbar^2}{2m_{eff}} \left(\frac{\pi n}{L} \right)^2 \quad (2).$$

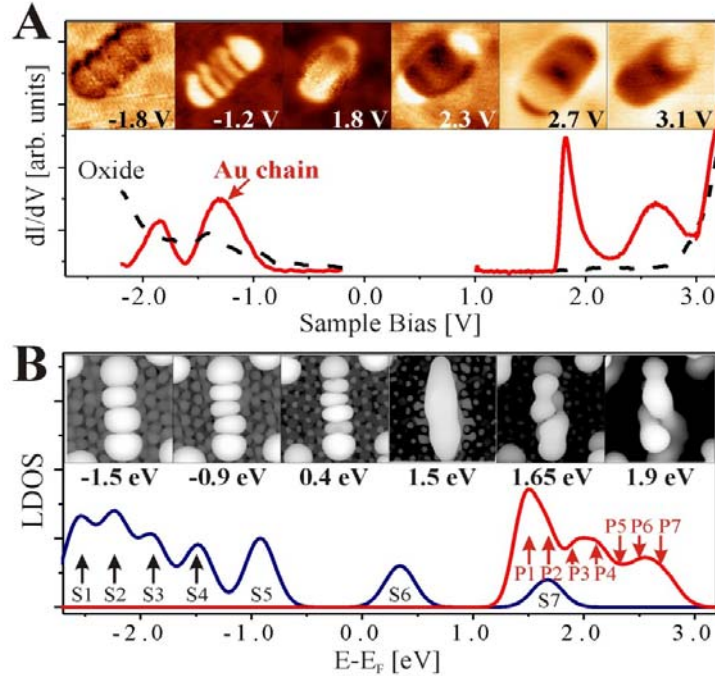


Figure 9 (A) Conductance spectra of an Au₇ chain and the bare oxide film. The insets display dI/dV maps taken at the peak positions of the respective spectrum (5×5 nm²). (B) Calculated LDOS for an Au₇ chain. The blue line denotes the seven Au 6s-like QWS (termed S1-S7), while the red line depicts the 6p state density. The quantized nature of the 6p states is not resolved due to the small energy separation between adjacent levels. The energy position is however marked by arrows (P1-P7). The calculated orbital shapes for the 4th - 6th s-like and the 1st - 3rd 6p-like QWS are shown as insets [39].

The electronic signature of ultra-small Au aggregates discussed above has been reproduced experimentally by STM conductance spectroscopy (Figure 8, D-F) [39]. The Au dimer displays one dI/dV maximum at +2.6 V, while two maxima at +2.3 / +3.0 V are detected for the trimer. These peaks are compatible with the lowest p_z -like QWS in the Au aggregates. This assignment is supported by dI/dV maps of the trimer taken at the respective peak positions. While a homogeneous dI/dV intensity distribution is revealed for the lower state, reflecting the constant density probability of the ground-state p_z orbital, a region of suppressed conductance marks the nodal plane in the first excited p_z -derived state (Figure 8F). Note that the LUMO of the monomer was not detected, most likely because of the overlap of this state with the alumina conduction band.

Also conductance spectra of longer Au chains are in agreement with the electronic structure sketched above [39,37]. In positive-bias spectra, two dI/dV peaks are ob-

served for Au₄ and Au₅ chains, while three maxima are resolved for the gold heptamer (Figure 9) [40]. Based on their energy position, the maxima are assigned to the unoccupied 6p_z-like QWS, the onset of which has been determined to 1.8 eV. As the energy spacing between adjacent 6p_z-levels is relatively small, the corresponding dI/dV maps do not show the unperturbed symmetry of isolated QWS but always result from a superposition of adjacent levels. In contrast to ultra-small aggregates, filled QWS are detected in the longer Au chains as well as the tetramer displays two dI/dV peaks below E_F, whereby the upper one at -1.1 V (the HOMO) exhibits three electron-density maxima and two nodal planes along the chain axis (Figure 10). The HOMO is therefore assigned to the third *s*-like QWS, being characterized by three density maxima. Assuming double occupancy of all QWS below the Fermi level, the total number of *s*-electrons in this ad-chain would be six. While four electrons are provided by the incoming Au atoms, the other two originate from the NiAl support, rendering the Au₄ chain twofold negatively charged. With the same arguments, the Au₅ chain was found to contain three extra electrons, as its HOMO at -1.6 V exhibits four intensity maxima and is thus assigned to the 4th QWS. Only five of the eight *s*-electrons are intrinsic to the Au atoms in this case, while the other three originate from the substrate again. For the Au₇, being the longest chain observed experimentally, the fourth and fifth QWS are detected at -1.8 and -1.3 V, respectively. In agreement with the particle-in-the-box model, the lower state displays four and the higher five density maxima along the chain axis in the dI/dV maps (Figure 10). The Au₇ chain has consequently five occupied QWS carrying ten *s*-electrons in total, which brings the number of transfer electrons from the NiAl to three again. It should be mentioned that no six-atom chains have been identified in the experiment, which might be explained with an unfavorable magnetic ground state of the linear Au₆ arising from an unpaired electron at E_F.

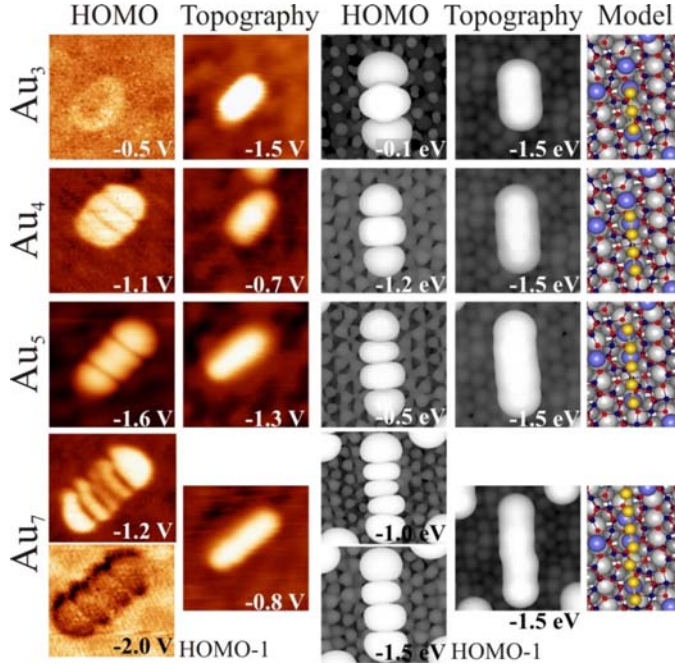


Figure 10: Experimental and calculated topography, HOMO shape and model structure for Au_3 to Au_7 chains on alumina /NiAl(110). All images are $5.0 \times 5.0 \text{ nm}^2$. The HOMO-1 for the Au_7 is shown in addition. Measured chain lengths are 9 Å, 12 Å, 15 Å and 22 Å; calculated distances between first and last chain atom amount to 5.3 Å, 7.8 Å, 10.5 Å and 15.5 Å. To compare theoretical and exp. lengths, 2-3 Å should be added to both sides of the chain to account for the diffusivity of the 1D orbitals [37].

Both, the experimental and theoretical behavior of s -like QWS in different Au chains are in good agreement with the particle-in-the-box model sketched above. Fitting the computed level energies to a parabolic dispersion relation yields a potential depth of $E_0 = -2.65 \text{ eV}$ and an effective electron mass $m_{\text{eff}} = 0.85m_e$. It is interesting to note that Au chains assembled directly on the metallic NiAl(110) support have a smaller electron mass of $0.5 m_e$ [52,51]. This finding indicates higher electron-mobility in the metal-supported chains, despite a somewhat larger Au-Au distance in that case (2.89 Å on NiAl versus 2.6 Å on alumina). The difference reflects the role of indirect coupling between the Au atoms, mediated by electronic states in the NiAl substrate. Naturally, this contribution is missing on the insulating alumina film [53].

2.4 Development of two-dimensional metal islands on oxide thin films.

The charge transfer through a thin oxide spacer prevails also for larger Au aggregates and keeps controlling their geometry and electronic structure. On 2ML MgO/Ag(001) films, for example, gold first forms flat, single-layer islands and develops a nearly complete wetting layer with increasing exposure (Figure 11) [15]. The formation of 2D islands is in sharp contrast to the 3D growth that is typically observed on bulk oxides [26,54,16]. It reflects the tendency of gold to increase the contact area with the oxide film, as this maximizes the charge transfer into the gold affinity levels and therewith the strength of the metal-oxide adhesion. Similar to Au monomers and chains, the reinforcement of the Au bonding results from increased electrostatic and polaronic interactions upon charge transfer [55]. As a rough number, the average charge transfer per ad-atom has been calculated to be $-0.2|e|$ for a close-packed Au layer on 2ML MgO/Ag(001) [56].

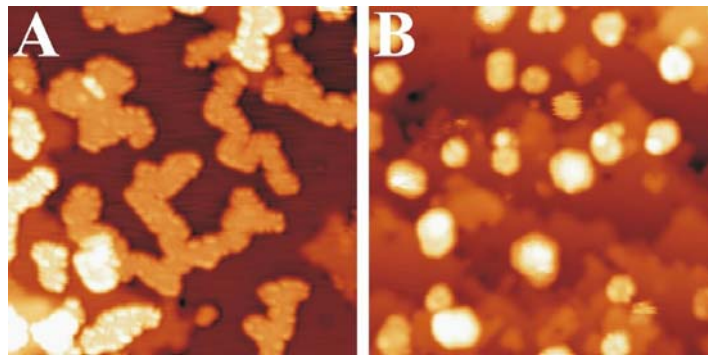


Figure 11: STM images of Au deposits on (A) 3 ML and (B) 8 ML MgO/Ag (001) ($30 \times 30 \text{ nm}^2$). Due to the charged-mediated adhesion, Au wets the ultra-thin MgO film. In the case of thicker films, the electron transfer is inhibited and 3D gold particles form on the oxide surface [15].

Especially in larger 2D gold islands, the excess electrons are not homogeneously distributed but show a preference to accumulate at the island perimeter [57]. The reason for this particular charge distribution is similar to the one that leads to the development of 1D chains at small atom numbers. The excess electrons repel each other, which increases the internal Coulomb repulsion in the island and hence the total energy. To minimize this Coulomb term, the extra charges maximize their mutual distance, which promotes their localization along the island edges. The presence of a negatively charged perimeter can be deduced directly from STM conductance maps of the 2D Au islands, as shown in Figure 12. Especially around the Fermi level, the island edges appear with enhanced dI/dV contrast, indicating a higher density of states as compared to the island interior. The contrast enhancement at the edge is compatible with specific edge states that enable accommodat-

tion of the extra electrons that have been transferred through the oxide film into the gold sheets. This mechanism has been corroborated by tight-binding DFT calculations, which allow for an explicit treatment of the atomic structure and the edge configuration even of extended metal nanostructures [57]. Also, the computed charge density plots unambiguously demonstrate the localization of electronic states along the island perimeter (Figure 12). These states are able to store one extra electron per low-coordinated edge atom, and get filled up with transfer electrons although the island interior remains neutral. This charge localization in the low-coordinated edge atoms renders the 2D Au islands supported on thin oxide films particularly interesting for adsorption and chemical reactions involving electron-accepting molecules (Lewis acids) [58].

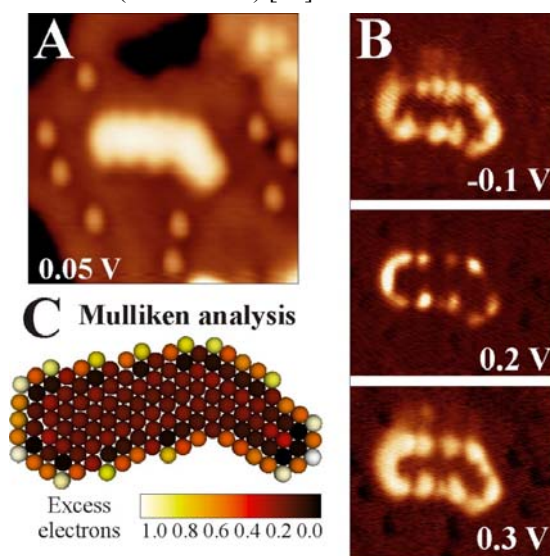


Figure 12: (A,C) STM topographic image and dI/dV maps of an planar Au island on 2 ML MgO/Ag(001) taken at the indicated bias voltage ($U_S = 0.2$ V, 25×25 nm²). (C) Corresponding charge distribution as calculated with a Density Functional Tight Binding approach [57].

Also for flat Au islands on MgO/Ag(001), STM conductance spectroscopy can be exploited to determine their charge state [56]. As discussed before, the development of well-defined QWS is the necessary precondition for this analysis, whereby symmetry and electron filling of the QWS have to be compared to the findings in neutral aggregates. As electron confinement in a 2D potential is more sensitive to structural irregularities, Au islands with suitable QWS need to be highly symmetric and free of defects.

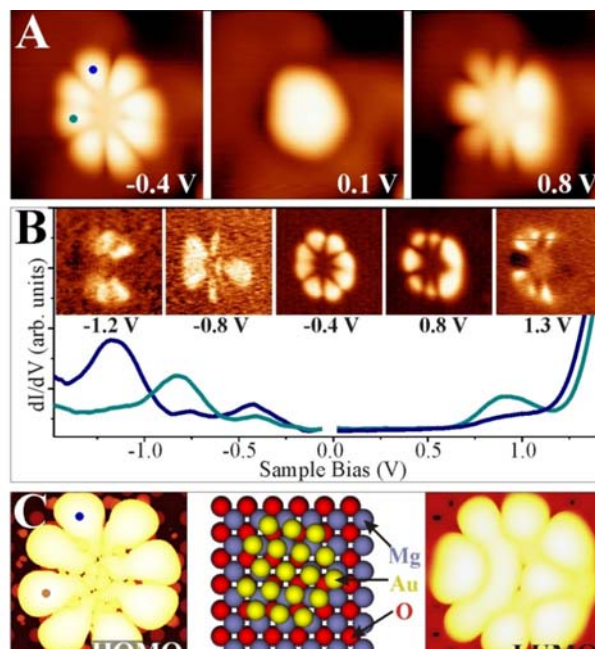


Figure 13: (A) Topographic and (B) dI/dV image of a symmetric Au cluster on 2 ML MgO/Ag(001) taken at the given sample bias ($3.9 \times 3.9 \text{ nm}^2$). The corresponding dI/dV spectra are shown in addition (blue and cyan curves: top and left part of the cluster). (C) Calculated HOMO and LUMO shape, as well as structure model of an Au₁₈ cluster on MgO/Ag(001). Perfect match between experimental and theoretical cluster properties indicate the identity of both aggregates [56].

A particularly instructive example shows an ultra-small Au cluster with $\sim 10 \text{ \AA}$ diameter and $0.8\text{-}0.9 \text{ \AA}$ apparent height grown on an 2ML MgO/Ag(001) film (Figure 13) [56]. In low-bias STM images, mainly the cluster morphology is revealed, as no eigenstates of the aggregate are available in the probed energy window. At slightly higher bias, the apparent cluster height doubles and flowerlike protrusions emerge in the image. This bias-dependent contrast change provides evidence that tunneling is now governed by the electronic and not the topographic properties of the nanostructures. More precisely, a distinct eigenstate, the LUMO of the Au aggregate, becomes accessible to the tunneling electrons, and dominates the image contrast at positive bias. A similar observation is made at negative bias, when the Au HOMO moves into the bias window and a comparable ‘nano-flower’ becomes visible in the STM. The two observed QWS closely resemble the eigenstates of a free-electron gas confined in a 2D parabolic potential (Figure 14) They are derived from the Au 6s states of the participating atoms and preserve their characteristic symmetry, as they neither mix with the states of the wide-gap oxide material nor with the Au 5d and 6p states positioned of much lower or higher energy, respectively [43,59]. The symmetry of the states is defined by the angular momentum

quantum number m , being a measure of the number of nodes in the 20 electron density probability [60]. The two lowest QWS in Figure 13 feature four nodal planes, which corresponds to an m of 4 or, equivalently, to a state with G-symmetry.

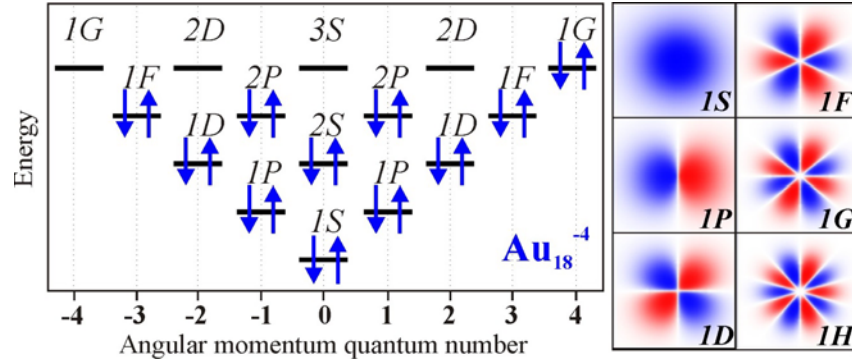


Figure 14: Energy levels (left) and orbital shapes (right) of the free-electron eigenstates in a 2D parabolic potential. The electron occupancy determined for a particular Au cluster on 2ML MgO/Ag(001) (here the Au₁₈ cluster) is depicted by arrows.

Again, the STM reveals not only the symmetry of the eigenstates, but via the spectroscopic channel also their energy position. For the Au cluster shown in Figure 13, the HOMO and LUMO are clearly identified as dI/dV peaks at -0.4 and +0.8 V, respectively, separated by a region of zero-conductance of 1.0 V width. Also higher QWS show up in the dI/dV spectra of the cluster. The HOMO-1 at -0.8 V and the HOMO-2 at -1.2 V are both of *P*-symmetry with the nodal plane pointing in two orthogonal directions. Note that higher and lower states cannot be resolved as an increasing overlap with the MgO electronic states renders their identification difficult.

With this experimental input, the electronic structure of the gold nanoisland and more importantly its charge state can be determined by comparing the measured orbital shapes with DFT calculations for possible sample clusters [56]. Following an extensive theoretical search, the experimental signature shown in Figure 13 could be matched on the properties of a planar Au₁₈ cluster. Its structure is derived from a magic-size Au₁₉ cluster with one missing corner atom. In agreement with experiment, the HOMO and LUMO are two *1G* orbitals located in the 5th shell of the harmonic potential, whereas the HOMO-1 and HOMO-2 are the *2P*-like QWS states in the 4th shell (see level scheme in Figure 14). The missing atom with respect to a symmetric Au₁₉ gives rise to a slight asymmetry in the orbital shapes that becomes particularly evident for the LUMO. Counting the number of orbitals from the *1S*-like ground state to the *1G* HOMO, as plotted in Figure 14, we find eleven filled valence states for the Au₁₈ cluster being occupied by a total number of 22 *s*-electrons. As each of the 18 Au atoms adds only a single *6s* electron to the delocalized QWS, there is a difference of four electrons to the total electron count

determined by experiment. As discussed in detail for the Au chains, the missing four electrons are introduced via charge transfer from the MgO/Ag interface into the Au island. This charging effect is corroborated by a DFT Bader analysis, yielding a value of $-3.54|e|$ for the Au_{18} cluster, but matches also the average transfer of $0.2|e|$ per atom as calculated for dense-packed Au layers on thin MgO films [56].

Similar procedures have been carried out for many other Au aggregates on the MgO/Ag(001) system [56]. In all cases, a negative charging has been revealed, verifying the charge-mediated binding concept for Au islands on thin oxide films [38,49,7]. The number of transfer electrons was found to be proportional to the atom number in the 2D cluster or, synonymously to the interfacial contact area (Figure 15). Interestingly, the accumulated charge per Au atom is generally lower in 2D aggregates as compared to 1D chains, which might be rationalized by the higher efficiency of the linear systems to distribute the excess electrons and lower the internal Coulomb repulsion [48]. The energetic preference for chains diminishes, however, for clusters containing more than 6-7 atoms, inducing a crossover to 2D island shapes and later to 3D structure. It should be mentioned that also the HOMO-LUMO gap shows a strong dependence on the atom number per cluster (Figure 15). Whereas Au aggregates containing 10-15 atoms have experimental gap sizes of around 1.5 eV, the HOMO-LUMO gap closes for more than 100 atoms in the cluster, reproducing earlier results for Au clusters on TiO_2 [61]. The gap size hereby follows the inverse cluster area Ω according to $E_g \propto \Omega^{-1}$, as expected for the energy separation of eigenstates in a 2D harmonic potential [60,43].

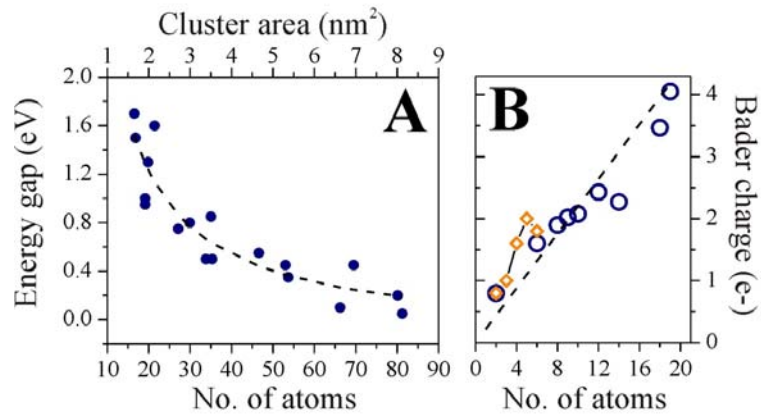


Figure 15: (A) Experimental HOMO-LUMO gap for differently sized Au clusters on MgO/Ag(001). The atom number is deduced from the measured particle area Ω , using DFT results as a reference for the de-convolution procedure. The dashed line is a fit of the data to the inverse cluster size. (B) Calculated number of excess electrons in linear (diamonds) [48] and 2D Au clusters on 2ML MgO/Ag(001) [56]. The line depicts the charge accumulation of $0.2|e|$ per atom, being computed for a compact Au layer on 2 ML MgO/Ag(001).

In summary, the charge-mediated binding scheme of gold to oxide films is closely related to the possibility to transfer electrons through the insulating spacer. The dominant transport mechanism is electron tunneling from the Fermi level of the metal substrate through the oxide layer. The tunneling probability depends exponentially on the oxide thickness, and to a smaller extent on the gap size, as already discussed by Cabrera and Mott [55,62]. As an interesting consequence the growth regime of Au on thin oxide films might be altered simply by increasing the film thickness until tunneling transport becomes impossible (Figure 11) [15]. Whereas only 2D islands are found on 3ML MgO/Ag(001) films, a dimensionality crossover to 3D particles occurs on 8ML films that do not support charge transfer anymore [16]. These experiments have been reproduced by DFT calculations, addressing the shape of Au₈ clusters on 2 and 5ML thick MgO/Ag(001) films [55]. With increasing oxide thickness, the amount of charge transfer was found to decrease by 50%, causing the interfacial adhesion to drop from 0.7 to 0.35 eV per interfacial atom. As a result, the initially planar Au₈ cluster turned 3D on the thick film in order to increase the number of Au-Au bonds and to counterbalance the loss in interfacial adhesion. Both experiments and theory therefore confirm the importance of charge transfer in determining the growth shape of metals on thin-film systems.

2.5 Metal growth on doped oxide materials.

The former paragraphs have demonstrated how the equilibrium shape of metal particles on oxide supports depends on the charge state of the deposits. It turned out that charged species, either single atoms or small aggregates, tend to bind stronger to ionic oxides, as they exhibit additional electrostatic and polaronic interaction channels that are not available for neutral entities [55,28]. However, the concept of charge-mediated control of the metal-oxide adhesion seems to be restricted to ultra-thin films, as the extra electrons are provided by a metal substrate and need to tunnel through the insulating spacer layer. In contrast, the request to tailor the equilibrium shape of metal particles becomes particularly large on bulk oxides as used in heterogeneous catalysis, as the chemical properties of metal-oxide systems was shown to depend sensitively on the particle shape [63-66]. The relation between chemical reactivity and geometry of the active metal species has been explored in detail for gold [8]. Raft-shaped Au islands on iron oxide, for example, have been identified as the active entities in the low-temperature oxidation of CO [67,68]. Also in the Au/TiO₂ system, bilayer deposits turned out to be the most active [61,69]. Both results suggest a special role of the perimeter sites of metal deposits, which enable molecules to interact simultaneously with the metal and the oxide support. As those sites are most abundant on flat metal islands, a close interrelation between structure and reactivity is not surprising. We note in passing, that the shape affects also other fundamental properties of metal deposits,

e.g. their electronic structure and optical response [70,71], which renders a careful shape control relevant for applications in microelectronics, nano-optics and photocatalysis as well.

One possibility to extend the concept of charge-mediated particle growth to bulk oxides is the insertion of suitable charge sources directly into the oxide material, preferentially into a near-surface region to allow for charge exchange with adsorbates. By this means, all advantageous effects of charge control could be maintained for oxide slabs of arbitrary thickness. The fundamental approach to insert charge centers into a material is doping, and the underlying concepts have been introduced and brought to perfection already in the mature field of semiconductor technology. Surprisingly, the art of doping is less advanced what oxide concerns, which relates to a number of peculiarities in these materials. Oxides are subject to self-doping either by native defects or unwanted impurities, the concentration of which is difficult to control experimentally [72]. Both, lattice defects and impurity ions may adopt different charge states in the oxide lattice [73,74], a variability that leads to pronounced compensation effects and is less common in semiconductors. And finally, the dopants may be electrically inactive in a wide-gap insulator, as thermal excitation is insufficient to rise the electrons from defect states into the bulk bands. As a result, the excess charges remain trapped at the host ions and are unavailable for charge transfer. The following examples demonstrate, however, that doping is a versatile approach to control the growth of metals even on bulk-like oxide materials [75-77,18,17,78,79]. The underlying concepts are thereby similar to the charge-transfer picture developed for thin films before.

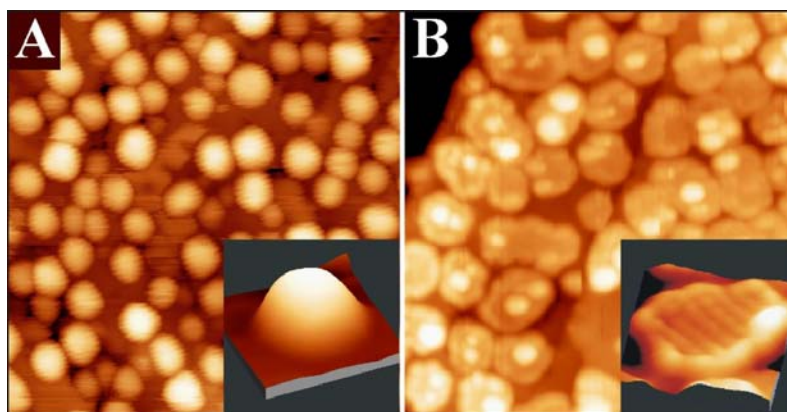


Figure 16: STM images of 0.7 ML Au dosed onto (a) pristine and (b) doped CaO films (4.5 V, $50 \times 50 \text{ nm}^2$). The insets display close-ups of two characteristic particles (-5.0 V, $10 \times 10 \text{ nm}^2$)

In general, doping is carried out with impurity ions that adopt either a higher or lower valence state than the substituted ions in the oxide lattice. In rare case, also charge-preserving doping is realized, and geometric and strain effects and not

charge-transfer become relevant in these cases. Whereas high-valence dopants may serve as charge donors and provide extra electrons, undervalent dopants have acceptor character and may accommodate electrons from suitable adsorbates. Based on the above considerations we now expect that charge donors in an oxide lattice have a similar influence on the particle shape as the metal support below a thin oxide films.

The impact of doping on the growth morphology of gold has first been realized for crystalline CaO(001) doped with Mo in the sub-percent range [80]. On the doped oxide, the gold was found to spread out into extended monolayer islands, while the conventional 3D growth regime prevailed on the pristine, non-doped material (Figure 16). Evidently, the donor character of the Mo dopants is responsible for the 2D growth-morphology, as the bare CaO(001) surface interacts with gold only weakly. The Mo⁺ impurity ions mainly occupy Ca substitutional sites and, in the absence of gold, adopt the typical 2+ charge state of the rocksalt lattice in order to maintain charge neutrality. In the 2+ configuration, four Mo *4d* electrons are localized in the dopant, three of them occupying ($t_{2g}-\alpha$) crystal field states and one sitting in a ($t_{2g}-\beta$) level close to the upper end of the CaO band gap (Figure 17) [80]. Especially the latter one is in an energetically unfavorable position and therefore susceptible to be transferred into an acceptor state with lower energy. Such states are indeed provided by the Au atoms that exhibit half-filled *Au 6s* levels at lower energy. DFT calculations therefore reveal a spontaneous transfer of the top-most Mo *4d*-electron into the Au 6s affinity level, resulting in the formation of an Au⁻ anion (Figure 17). As discussed for the thin films, the charged gold experiences reinforced bonding to the CaO surface, reflected by the increase of the binding energy from ~1.5 eV without to ~3.5 eV with Mo dopants in the film. We emphasize that the charge transfer does not require the presence of a Mo ion in the surface and remains active over relatively large Mo-Au distance of up to ten atomic planes.

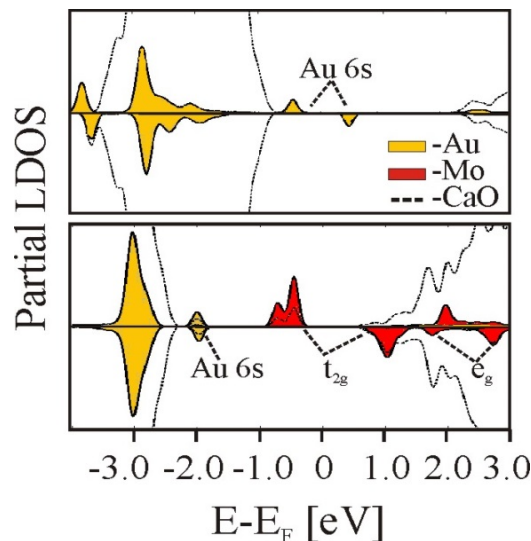


Figure 17: PBE projected state-density calculated for non-doped (top) and doped (bottom) CaO films in presence of an Au adatom [80].

The increase of the metal-oxide adhesion due to dopant-induced charge transfer fully explains the 2D growth regime of gold observed in the experiment. Gold tends to wet the CaO surface in an attempt to maximize the number of exchanged electrons, hence the interfacial interaction. Further DFT calculations suggested that also a Mo^{3+} species that has already lost one electron remains a potential donor, as two of the residual d -electrons are still higher in energy than the Au 6s affinity level [81]. Consequently, even a second and a third electron may be transferred into the ad-metal, leaving behind thermodynamically stable Mo^{4+} and Mo^{5+} ions in the CaO lattice. It is this behavior of the Mo ions that is responsible for the robust donor behavior of Mo-doped CaO [80].

The presence of suitable dopants is, however, not the only requirement for a stable donor characteristic, the interplay between dopants and host oxide determines the redox activity. This shall be demonstrated for two similar systems, Cr-doped MgO and Mo-doped CaO, which still exhibit an entirely different behavior [81-83]. Chromium has a similar electronic structure as Mo, i.e. the same number of d -electrons, but is a $3d$ and not a $4d$ metal. Surprisingly, it is unable to influence the Au growth behavior on the MgO support (Figure 18). Even at a high Cr concentration, the 3D growth of gold prevails and hardly any 2D islands are found on the surface. The reason for this poor behavior is the low energy position of the $\text{Cr } t_{2g}$ levels in the MgO band gap, which originates from a substantial stabilization of the $\text{Cr } 3d$ -electrons in the MgO crystal field. Note that the crystal field in MgO is substantially stronger than in CaO, due to the reduced lattice parameter [84]. In addition, the ionization energies of Cr atoms are higher than for Mo, which makes formation of Cr^{4+} and Cr^{5+} ions energetically more expensive [85]. As a result, Cr

is able to donate at maximum one single electron to gold, which compares to three for the Mo dopants in CaO [81].

Moreover, this electron may not even reach the ad-metal, because it is likely to be captured by parasitic electron traps that are present in real oxides. Typical electron traps are cationic vacancies, e.g. Mg defects, domain boundaries, or dislocation lines [86]. The cation-defects (V -centers) preferentially develop in oxides with a large number of high-valence dopants, as they are able to compensate the augmental charge state of the impurities with respect to the intrinsic ions [84]. According to DFT calculations, the formation energy of electron-trapping (V -centers decreases from more than 8 eV in bare CaO and MgO to 1.0-1.5 eV in the presence of high-valence dopants [81]. As a result, internal compensation effects become favorable, in which every dopant in the lattice produces a balancing vacancy. Whiles this internal compensation remains insufficient to cancel the donor potential of Mo ions, it annihilates the effect in Cr-doped MgO. Consequently, no charge-mediated changes in the Au growth morphology are observed for Cr-MgO, although the effect is huge for the Mo-doped CaO (Figure 18). One conclusion of these results is that the donor behavior of a transition-metal doped oxide cannot be predicted by simple valence arguments but needs to be checked in every single case.

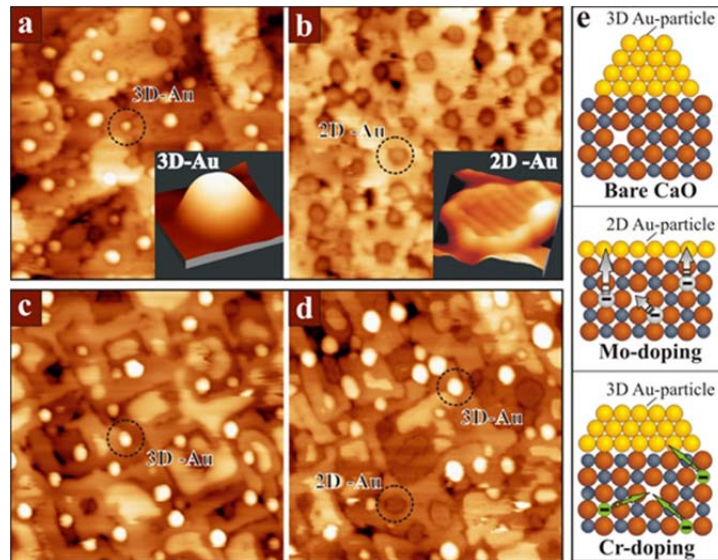


Figure 18: STM images of (a) bare and (b) Mo-doped CaO(001) films of 60 ML thickness after dosing 0.5 ML of Au ($60 \times 50 \text{ nm}^2$, +6.0V). The 2D Au islands appear as depressions on the insulating oxide, because electron transport into the gold is inhibited at the high positive bias needed for scanning. The insets show typical 3D and 2D islands taken at lower bias (3.5 V, $10 \times 10 \text{ nm}^2$). Similar measurements on (c) bare and (d) Cr-doped MgO(001) films of 20 ML thickness. The particle shape is not affected by the dopants in this case. (e) Ball models explaining possible charge-transfer processes between the doped oxide and the ad-metal and their influence on the particle shape.

The influence of overvalent dopants on the equilibrium morphology of metal particles can, to a certain extent, be annihilated by undervalent dopants in the oxide lattice (Figure 19) [87,88]. Dopants with lower charge state generate holes in the oxide electronic structure that are able to trap the extra electrons provided by the charge donors. This mutual compensation between donors and acceptors has been explored for CaO films co-doped with Li and Mo ions [89]. At low Li concentration with respect to Mo, most of the Au particles still adopt 2D shapes, indicating a prevailing charge transfer into the gold. With increasing Li doping level, however, more deposits turn 3D, as the ad-particles are unable to accumulate enough excess charges from the Mo donors (Figure 19C,D). The extra electrons are trapped by lattice defects that arise from the presence of Li in the lattice. Every monovalent Li^+ ion sitting in Ca^{2+} substitutional sites produces a deep hole in the $\text{O}2p$ states of an adjacent oxygen forming an effective trap for the Mo 4d electrons. As a result, charge transfer to the surface ceases at a critical Li doping level and the Au deposits adopt the typical 3D geometry of pristine CaO films.

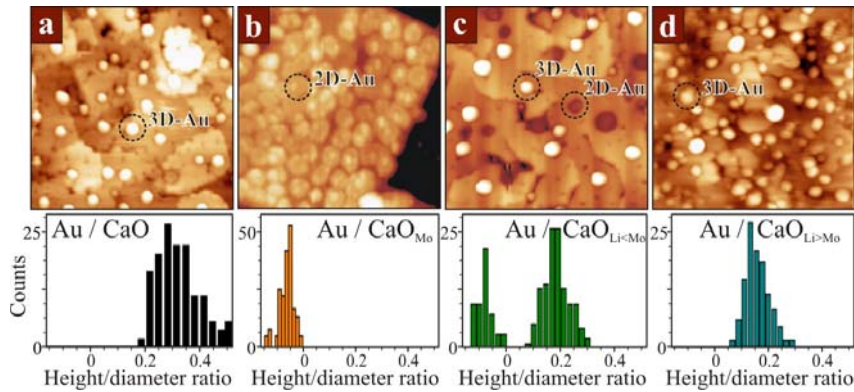


Figure 19: STM images of 0.5 ML Au deposited onto (A) pristine CaO, (B) doped with 4% Mo, (C) doped with 4% Mo + 2 % Li and (D) doped with 4% Mo + 8 % Li ($50 \times 50 \text{ nm}^2$, 6.0 V). Note that monolayer Au islands in (B) and (C) appear as depressions at high sample bias. Histograms of the particle shapes (height-to-diameter ratio) are plotted below. Note the transitions from 2D to 3D particles when the overvalent doping with Mo in (B) is balanced with increasing amounts of monovalent Li impurities.

We note that pure hole-doping could not be realized in the experiments so far. Neither MgO nor CaO films, doped exclusively with Li, were found to alter the morphology and electronic structure of gold, and no sign for the generation of positively charge ad-species was obtained. This finding is in agreement with the occurrence of intrinsic compensation mechanisms in the oxides that remove the energetically unfavorable holes produced by the Li^+ species. Even in well-prepared oxide films and at perfect vacuum conditions, competing electron sources are present, such as electron-rich oxygen vacancies (F^0 centers) and donor-type adsorbates from the rest gas (water, hydrogen) [87,88,90,91]. Hole-doping of oxides as a

means to tailor the properties of metal ad-particles is therefore more difficult to realize than electron-doping with donor-type impurities.

Interestingly, the competition for excess electrons occurs not only in Mo and Li co-doped films but is observed also in the presence of electron accepting species on the oxide surface. Gold forms monolayer islands if deposited onto a Mo-doped CaO at vacuum conditions, but 3D particles if oxygen is present during growth. The reason is that O₂ molecules bound to the surface act as electron acceptors as well, and may trap charges in their O 2π* antibonding orbitals. These electrons are lost for the Au islands, resulting in a gradual transition from a 2D to a 3D growth regime with increasing O₂ partial pressure. Whereas in 5×10⁻⁷ mbar of oxygen, 50% of the Au islands still adapt monolayer shapes, all Au deposits turn 3D grown in an 5×10⁻⁵ mbar O₂ background. The interplay between the observed growth mode and the composition of the gas environment emphasizes the pivotal importance of excess electrons from donor species for the reactivity of oxides towards adsorption of metallic and gaseous species.

In summary, doped bulk oxides display in many aspects similar adsorption properties as ultra-thin oxide films. In both systems, excess electrons are transferred into the ad-species and open up specific charge-mediated adsorption schemes. Whereas for ultrathin oxide films, the extra electrons are provided by the metal substrate below, doped oxides contain intrinsic charge sources in the form of aliovalent impurity ions. Thin oxide films grown on metal single crystals are mainly of academic interest, as they provide easy access to the properties of oxide materials via conventional surface science techniques. Doped oxides, on the other hand, are of practical relevance for many processes in heterogeneous catalysis. As shown in this section, overvalent dopants are able to change the particles equilibrium shape from 3D to 2D, which is expected to change the reactivity pattern of the metal-oxide system. Moreover, charge transfer from electron-rich dopants might be a suitable pathway for the activation of small molecules, such as oxygen or methane. A possible activation mechanism would be the occupation of the antibonding orbitals, leading to a destabilization or even dissociation of the molecules. In a recent experiment, electron donation from Mo-impurities was shown to produce super-oxo (O₂⁻) species on a CaO surface, which might be a highly reactive precursor for subsequent oxidation reactions. Although the chemical reactivity of doped oxides is still subject of active research, it appears already that oxide doping forms a promising route to fabricate highly reactive and selective catalysts for the future.

3 CO adsorption on supported Au particles

The binding of molecules to specific sites of a metal nanoparticle is thought to determine the reactivity of metal/oxide systems used in heterogeneous catalysis. The model systems, described above, represent ideal objects to study the influence of

size, shape and charge onto adsorbed molecules. Given the large body of information on CO as an adsorbate, this molecule represents the probe molecule of choice. Figure 20 shows the range of frequencies CO typically shows when bound to Au in different oxidation states [92].

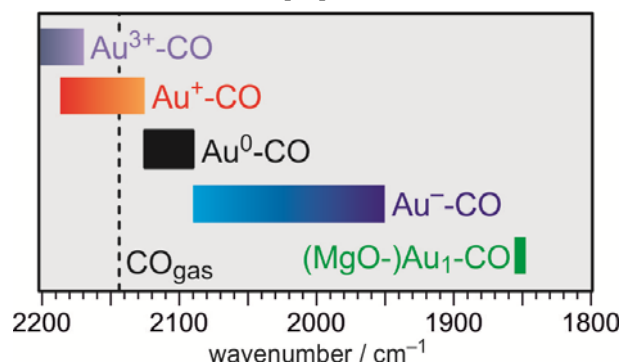


Figure 20: Connection between Au charge scale and the stretching frequency of adsorbed CO [92].

This knowledge, together with the possibility of imaging allows us to investigate, in detail, molecule-Au interactions. Before we discuss CO adsorption on nano particles we briefly discuss the frequencies of the outlier in Figure 20, i.e. the IR spectrum of CO interacting with a single Au atom [93]. When small amounts of Au are deposited on a 10 monolayer thick MgO(100) film, the Au atoms remain neutral, as conclusively shown via EPR measurements on the system [94]. CO adsorption leads to the appearance of a band at 1852 cm^{-1} in the IR spectrum, which has been identified with the help of a DFT calculation. The large shift of 285 cm^{-1} from the frequency of the gas phase CO arises because the Au 6s valence electron is strongly polarized away from the MgO surface due to Pauli repulsion with the oxygen ions to which the Au preferentially binds [94]. The concomitant transfer of electrons into the C-O anti-bonding $2\pi^*$ orbital leads to this dramatic weakening of the intermolecular bond, hence a redshift of the stretching frequency. This shift is even larger than for an Au atom residing on a color center holding one electron, i.e. there the shift is 220 cm^{-1} [93].

3.1 CO Adsorption on Au on Thin MgO/Ag Films.

Molecular species can also be identified directly on oxide-supports gold nanostructures, using low-temperature STM. For example, single CO molecules are imaged as circular depressions on the MgO surface (Figure 21a).

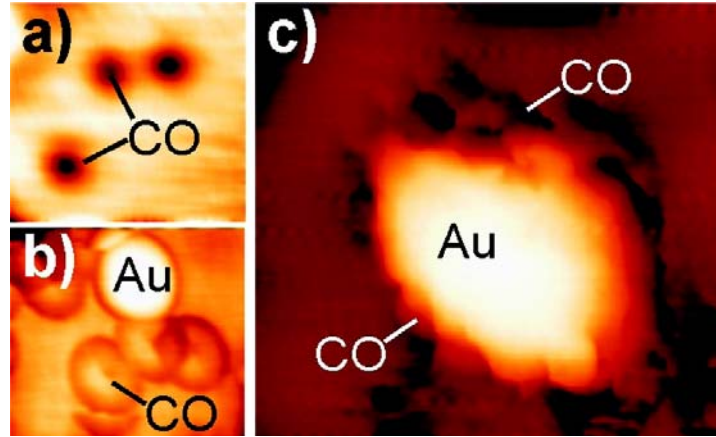


Figure 21: STM topographic images of CO molecules on 2 ML MgO/Ag(001) imaged with (a) a metallic and (b) a CO-covered tip ($3 \times 3 \text{ nm}^2$, 150 mV, 3pA). The CO(tip)–CO(sample) interaction leads to a ring-like appearance of the adsorbates in (b). (c) STM image of a CO-saturated Au island taken with a CO-covered tip ($4 \times 4 \text{ nm}^2$, 100 mV, 3pA). CO-induced contrast is only revealed at the perimeter of the Au island [66].

A similar imaging contrast is observed on most metal surfaces, where it originates from the absence of CO orbitals for tunneling transport close to the Fermi level (E_F) [95]. CO attachment to the tip gives rise to a distinct contrast change of the adsorbates, which now appear as dark rings of $\sim 8 \text{ \AA}$ diameter (Figure 21 b). This imaging mode enables CO identification even on corrugated surfaces, e.g. next to an Au deposit, where the tiny CO-induced depressions obtained with metallic tips are no longer detectable. Figure 21c shows a corresponding STM image of an Au island saturated with CO. Apparently, the CO-induced features are exclusively localized along the island perimeter, while the center remains adsorbate-free. An alternative method to identify CO molecules on the oxide surface is inelastic-electron-tunneling spectroscopy (IETS) with the STM [96-98]. The peak/dip positions observed in the second-derivative d^2I/dV^2 spectra correspond to the vibrational energy modes of the molecules. The CO vibrational mode with the highest excitation cross section in STM-IETS is the frustrated rotation [96]. Consequently, bias voltages of 45 mV have been chosen to identify CO molecules next to the 2D Au islands via their vibrational signature (Figure 22 a-d).

As mentioned before, no CO is visible on the aggregate in topographic images taken with a metallic tip. However, CO related loss signals emerge in the d^2I/dV^2 maps and produce a bright/dark brim around the island at positive/negative sample bias (Figure 22 c,d). Control measurements taken at bias values above or below the CO frustrated rotation did not produce any d^2I/dV^2 contrast (Figure 22 b). The localization of the inelastic signals along the perimeter therefore corroborates the CO attachment to edge and corner atoms of the Au islands. For comparison, we show similar information for a single Au atom with adsorbed CO. Here we see

a very similar spectral response indicating the a-top position of CO on the Au monomer (Figure 22 e-h).

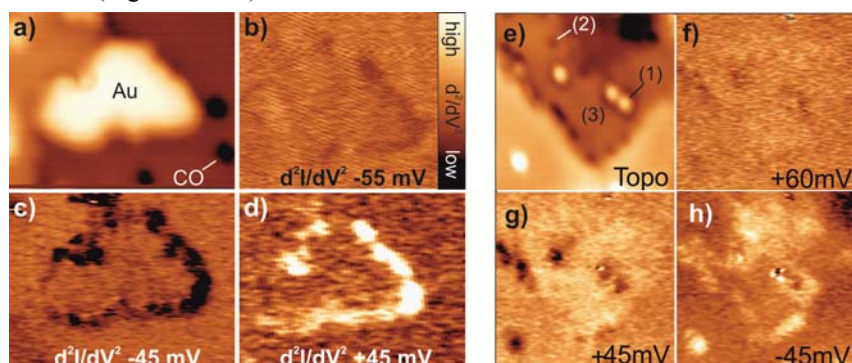


Figure 22: (a) STM topographic image and (b–d) corresponding second-derivative maps of a planar Au island saturated with CO ($7.0 \times 5.5 \text{ nm}^2$, 10pA). Due to the metallic tip state, the CO molecules are not resolved on the island but give rise to distinct energy-loss features at the island perimeter (c,d). The second-derivative contrast vanishes at bias voltages away from the CO vibrational modes (b), (e–h) corresponding information for single Au atoms [66,95].

The preferential CO binding to the island perimeter might be ascribed to two effects. On the one hand, the boundary atoms have a lower coordination than the ones enclosed in the Au plane. The same mechanism controls CO adsorption on stepped metal surfaces [99,100]. On the other hand, electrons transferred from the MgO/Ag-support are localized at the island perimeter, as discussed above and may alter the CO binding characteristic. According to DFT calculations, the coordination effect clearly dominates the CO binding position. Whereas CO adsorbs with 0.72 eV to 3-fold coordinated edge atoms of a negatively charged Au island on MgO/Ag(001), it is nearly unbound to the 5-fold coordinated atoms in the interior of island. A similar binding enhancement is revealed for edge versus inner atoms of a neutral Au_{12} island on bulk MgO [101]. The extra electrons localized on the perimeter of charged islands actually counteract this trend, as they impede charge donation from the CO 5σ orbital into the metal and hence increase the CO-Au repulsion [102]. Clearly, CO attaches to the island perimeter not because but in spite of the extra charge, and the binding preference with respect to the top facet is governed by the reduced coordination of the edge atoms.

This conclusion is supported by the experimental observation that CO adsorption modifies the charge distribution within the Au islands. The specific contrast at the rim of the islands (Figure 23a) disappears after CO dosage, when standing electron waves emerge in the island center (Figure 23b) [103]. Apparently, the CO removes the localized charges from the perimeter sites by pushing them into the interior of the island. Also this finding is in line with DFT results for charged Au_{12} clusters on MgO/Ag(001) [101].

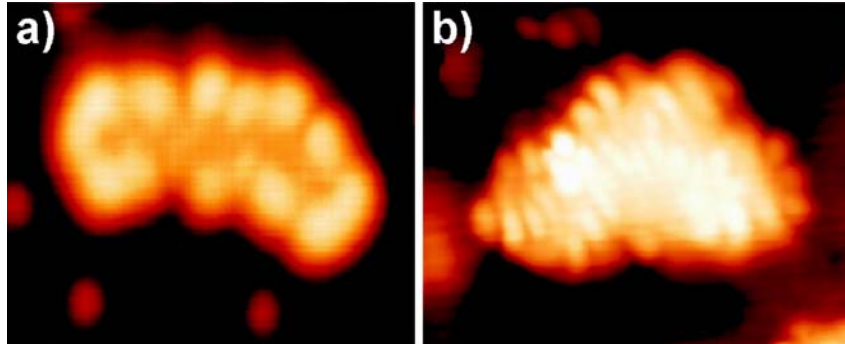


Figure 23: STM topographic images of (a) a bare (see also Figure 12) and (b) a CO-saturated Au island on 2 ML MgO/Ag(001) ($7.0 \times 5.5 \text{ nm}^2$, $V = 150 \text{ mV}$). Whereas the bare island is surrounded by a bright rim, indicating charge accumulation at the perimeter, the CO-covered island exhibits charge-density waves in the interior. The standing electron waves are due to electron displacement from the island boundary upon CO adsorption [66].

While on ultrathin films we resorted to IETS to probe the vibrations on adsorbed CO, on thick insulating films the CO binding properties have been studied with IRAS, whereas STM still provides information on the nucleation density and size of the Au aggregates. Figure 24a displays an STM topographic image of a 12 ML thick MgO/Mo film, being exposed to electrons to produce F^0 and F^+ centers. Those point defects that mainly form along step edges and misfit induced dislocation lines are the preferential Au nucleation sites on the oxide [104]. After dosing 0.05 ML Au at room temperature, Au particles develop on the surface that are one to two layers high and contain 30-50 atoms (Figure 24a).

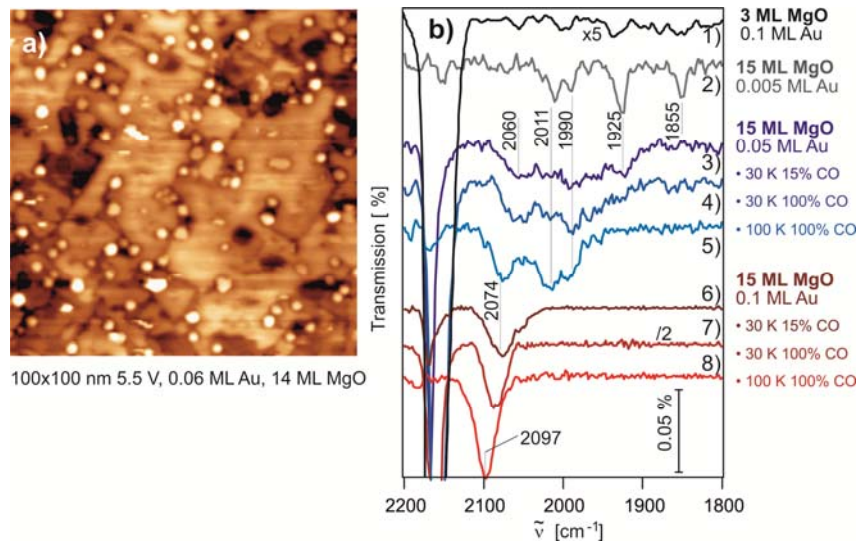


Figure 24: (b) Infrared absorption spectrum of CO adsorbed on a 3 ML MgO/Ag(001) film covered with 0.1 ML Au. (2–8) IR spectra taken on an electron-bombarded 15 ML thick MgO/Mo film covered with (2) 0.005 ML Au (CO saturation coverage, 100 K), (3) 0.05 ML Au (15% CO exposure, 30 K), (4) 0.05 ML Au (saturation coverage, 30 K), and (5) 0.05 ML Au (saturation coverage, 100 K). The spectra (6–8) were taken for 0.1 ML Au coverage and (6) 15 s CO exposure (30 K), (7) CO saturation coverage (30 K), and (8) after annealing the sample to 100 K [66].

For the IRAS experiments shown in Figure 24, Au deposition was carried out at 30 K, which increases the nucleation density and decreases the mean particle size. For the given coverage range of 0.1 to 0.005 ML Au, the size of Au deposits is expected to vary between a few tens of atoms down to monomers and dimers. The IRAS data (spectra 2-8) in Figure 24 show bands ranging from 2090 cm^{-1} all the way down to 1990 cm^{-1} as well as two isolated lines at 1925 and 1855 cm^{-1} . All bands are red-shifted compared to CO adsorbed on Au clusters on pristine MgO films, which are found between 2125 and 2100 cm^{-1} depending on the preparation conditions. The low-frequency lines that only occur at the smallest metal exposure (Figure 24 spectrum 2, gray line) are assigned to Au atoms adsorbed to regular terrace sites (1855 cm^{-1}) and F-centers (1925 cm^{-1}) on the basis of results discussed above. All other bands can be explained by CO bound to negatively charged Au aggregates located on top of electron-rich surface defects [92]. In particular, the noisy features at ~ 1990 and ~ 2011 cm^{-1} are suggested to originate from CO adsorption to ultra-small Au aggregates, e.g. dimers and trimers.

This assignment is corroborated by IR spectra taken at higher Au exposure (Figure 24, spectra 3-5, blue lines). In addition to the low-frequency bands discussed before, new blue-shifted lines emerge in the frequency range around 2060 cm^{-1} that shifts to 2070 cm^{-1} upon annealing to 100 K. For the highest coverage of 0.1 ML (Figure 24, spectra 6-8, red lines), the spectrum is dominated by a band at 2074 cm^{-1} , while the strongly red-shifted bands have disappeared. Annealing the system to 100 K induces again a blue shift of the line to 2097 cm^{-1} . Inspection of the two data sets shown in Figure 24, spectra 3-5 and 24, spectra 6-8 reveals that neither the intensity nor the line shape of the Au-related bands changes when the CO coverage is increased from 15% to 100% of the saturation value. Annealing the systems to 100 K, on the other hand, leads to a blue shift of the lines that reaches 15 cm^{-1} for the bands at 2060 (Figure 24, spectra 5) and 2080 cm^{-1} (Figure 24, spectra 8). At 100 K, CO desorbs from the MgO film as evident from the reduction of the MgO-related CO-stretch bands between 2150 and 2180 cm^{-1} . In general, the CO stretching frequencies experience a decreasing red shift with higher Au exposure and increasing cluster size, a phenomenon that can be rationalized in the following way. Assuming that each Au aggregate nucleates on a single color center and takes up one electron, the density of excess charges decreases in the larger particles, which reduces the amount of π -back-donation into the CO and hence the red shift of the stretch mode. A similar conclusion was drawn from CO adsorption experiments on charged gas-phase clusters, where the CO stretch [105] mode was found to increase when going from Au^- (2050 cm^{-1}) to Au^+ clusters (2150 cm^{-1}).

This simple picture needs, however, to be modified in view of the earlier discussion. CO binds to the low-coordinated sites of the charged Au aggregates, which accommodate the extra electrons as well. The amount of π -back-donation now depends on the ability of the cluster to distribute the charge away from the CO adsorption site to lower the Pauli repulsion with the CO. Naturally, this ability diminishes with decreasing particle size, causing the charge transfer into the CO $2\pi^*$ to increase.

Based on these considerations, the experimental IR bands may be assigned. The bands above 2060 cm^{-1} that shift in an almost continuous fashion with Au exposure are produced by particles containing a few tens of atoms, whose charge density changes only gradually with size. The quasi-discrete bands at 1990 and 2010 cm^{-1} , on the other hand, are characteristic for ultra-small clusters such as dimers. A direct assignment of these bands is difficult, as not only the size of the aggregate but also the nature of the oxide defect underneath determines the vibrational response. According to DFT calculations, Au dimers bound to F^0 -centers interact only weakly with CO and produce a red shift of the stretching frequency of 194 cm^{-1} , whereas on F^+ -centers the binding is sizable and the red shift is smaller (158 cm^{-1}). However, also negatively charged Au_3^- and Au_4^- clusters [101] produce a red shift of $\sim 175\text{ cm}^{-1}$. The experimental CO bands at 1990 and 2010 cm^{-1} are therefore compatible with several ultra-small Au clusters.

In summary, whereas, on ultrathin films, the ad-particles charge up due to an electron transfer from the support, the charging on thicker films is realized by an electron donation from defects. In both cases, the excess electrons give rise to unusual CO adsorption properties, as deduced from STM and IRAS measurements. On planar Au islands on thin MgO films, the CO exclusively binds to low-coordinated Au atoms along the island perimeter. The adsorption is accompanied by a redistribution of the cluster electrons away from the boundary toward the interior. On thicker films, Au charging gives rise to an increasing red shift of the CO stretch mode with decreasing particle size, reflecting the gradual filling of the antibonding CO $2\pi^*$ orbital. The occurrence of sharp separated lines in the spectra, hence, indicates the presence of Au aggregates with well-defined atom counts.

3.2 CO adsorption on Au on ultra-thin alumina and Iron Oxide Films.

In the following, we will briefly also discuss CO adsorption on Au particles supported on other supports, such as alumina and iron oxide thin films, as we have also discussed their structure in the first part of this section.

TPD experiments of CO adsorbed on Au, deposited onto a thin alumina film at room temperature, revealed two clearly resolved peaks, with the first peak at around 120 K and another located at a higher temperature, depending on the Au

coverage (see Figure 25) [106]. Based on CO desorption results for stepped Au single crystal surfaces [107,108], both peaks were attributed to desorption from gold particles. The morphology of the similarly prepared samples was studied by STM in another UHV chamber as a function of the Au coverage. At low coverages, gold forms very small clusters and even single atoms (see for example Figs. 3 and 7) if the sample has not been exposed to elevated temperatures. Apparently, gold species are found randomly distributed across the surface without preferential decoration of the line defects clearly seen in the bottom STM image in Figure 25. At high coverage, gold forms hemispherical 3D-nanoparticles about 3-5 nm in diameter. With increasing the Au coverage and hence the Au cluster size, the position of the high temperature peak gradually shifts from 210 K to 160 K, thus indicating a size effect such that small Au particles adsorb CO more strongly. In addition, the intensity of this CO desorption signal reached saturation at a fairly low coverage of gold and low exposure of CO, suggesting that CO only adsorbs on low-coordinated Au atoms, but not on the regular terraces. Increasing Au coverage basically leads only to the gradual development of flat (111) terraces on the gold particles, which bind CO less strongly.

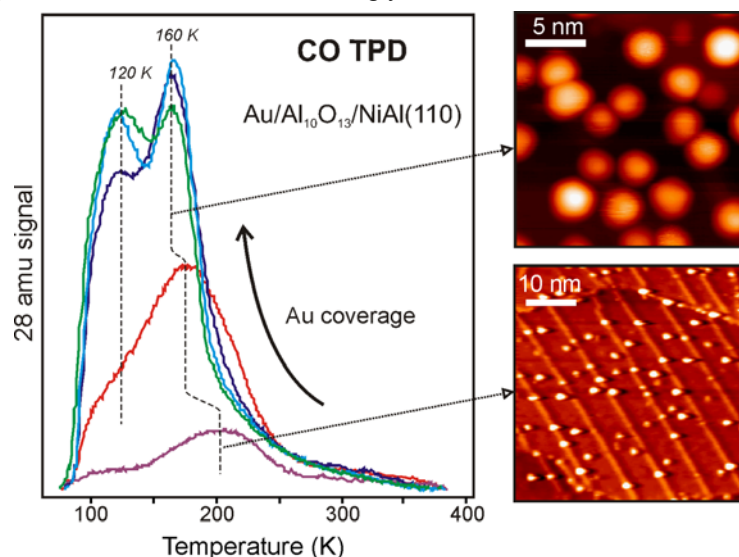


Figure 25: TPD spectra of CO exposed to Au/alumina film/NiAl(110) surface at 90 K as a function of Au coverage. Note that CO does not adsorb on the alumina film above 60 K. Typical morphology of similarly prepared surfaces is shown in the respected STM images taken in another experimental setup (see text).

On FeO(111) grown on Pt(111), the TPD data of CO adsorption again showed a strong size effect for Au particles deposited at ~ 90 K, with desorption states observed at temperatures as high as 300 K for the lowest gold coverage [109]. After annealing to 500 K, however, a reduction in signal intensity was observed and the

size effect is completely suppressed, as TPD spectra show two peaks similar to those observed in Figure 25 for alumina supported particles, independent of the amount of gold deposited. This finding indicates that after annealing particles have reached some critical size beyond which their adsorption behavior is size independent.

Au coverage dependent IRAS spectra taken after CO saturation (adsorption and deposition at 90 K) are shown in Figure 26 (left panel). At the lowest coverage studied here, a feature at 2165 cm^{-1} and a second at 2131 cm^{-1} are observed with approximately equal intensity. With increasing coverage, the low frequency peak gains intensity and shifts from 2131 to 2108 cm^{-1} , while the high frequency peak gradually attenuates. As shown in the right panel of Figure 25, annealing to 500 K in UHV results in a single state at 2108 cm^{-1} independent of the Au coverage. Bearing in mind the sintering effects of annealing, the peak at 2108 cm^{-1} can be straightforwardly assigned to CO adsorbing on metallic gold. The species giving rise to the peak at $\sim 2165\text{ cm}^{-1}$ is CO adsorbed on very small clusters, which - as shown above - undergo charge transfer. In this case a specific interaction with the support leads to positively charged Au species [110,46].

Interestingly, even monolayer islands formed on a FeO(111) film surface upon annealing display the same CO adsorption behavior as large, three-dimensional particles (see the STM images on the right side of Figure 26) or gold single crystals [109]. We thus concluded that the observed dependences are due to a higher percentage of highly uncoordinated gold atoms found for smaller particles, formed at low temperatures, which favor CO adsorption. Indeed, the single IRAS peak observed for the annealed samples did not shift and simply grew monotonically at increasing Au coverage. This supports the TPD results indicating no apparent change in the possible adsorption states for CO on monolayer islands as compared to large particles. Therefore, the results fit well the picture of exclusive CO adsorption on low coordinated surface atoms.

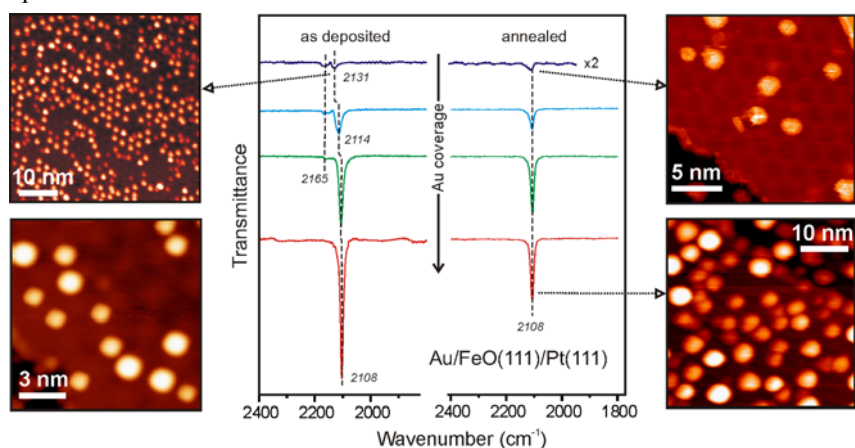


Figure 26: IRA-spectra of CO exposed to Au/FeO(111)/Pt(111) surface at 90 K as a function of Au coverage. Left panel: as deposited particles at ~90 K. Right panel: after annealing to 500 K in UHV. The STM images of the similarly prepared samples are shown. At very low temperatures (~10 K) and low coverages single Au atoms dominate the surface. Upon annealing, gold forms single-layer islands with about 2.5 nm diameter. At high Au coverage, only hemispherical 3D-nanoparticles are observed.

CO adsorption studies on Au deposited on alumina and iron oxide films performed in our group clearly show stronger CO binding on small particles. For the smallest Au coverage, CO may desorb at temperatures close to 300 K, which is in the temperature range of working Au catalysts for low temperature CO oxidation and has never been observed for Au single crystals. The presence of such a state is likely due to the presence of highly uncoordinated gold atoms.

Inspection of CO TPD spectra collected for gold particles deposited on various oxide [111] and carbon [112] films show that, for a given particle size (~ 3 nm as measured by STM), the interaction of CO with gold particles on different supports is virtually identical. However, the finding that annealing strongly attenuates size effects indicates that the nature of the support and its defect structure may be critical for nucleation, growth, and stabilization of very small Au clusters.

4 Nucleation and bonding of Au on chemically modified oxide surfaces

In section 2 we demonstrated the enormous potential of combining surface science experiments with DFT calculations in providing details about the interplay between electronic and structural properties of oxide-supported Au atoms, clusters and particles. Catalysis of supported gold strongly depends on these parameters, in particular on the particle size and the structure of the Au-support interface, and it is at the heart of catalyst preparation/synthesis to develop recipes that allow those units that are responsible for catalytic activity to be stabilized on the catalysts' surface. Indeed, much of the recent interest in gold surface chemistry arose from Masatake Haruta's observation of the unusual catalytic activity of highly dispersed Au supported by oxides, after finding a preparation method that resulted in stable, nano-sized Au particles [113]. In most cases, catalyst synthesis involves at least one wet-chemical preparation step, which adds some degree of chemical complexity to the systems that is typically not covered by surface science experiments carried out under ultrahigh vacuum conditions.

In the following we present two examples of surface science investigations into gold nucleation and bonding on oxide surfaces, which attempt to include some of the complexity of a real-world catalyst. The first one investigates the specific role of hydroxyl groups present on an oxide support on the morphological and chemical properties of Au nanoparticles. The second example presents an approach to study the preparation of an oxide-supported gold model catalyst using a single-

crystalline oxide support in combination with a wet-chemical preparation procedure.

4.1 Gold nucleation at hydroxyl groups.

We have chosen to use MgO(001) as a model surface to investigate the effect of hydroxyl groups on the properties of supported Au particles. Along the lines described in the previous sections, MgO(001) films were grown on a Ag(001) or Mo(001) substrate, but thicker films on the order of 10-15 ML thickness were used to exclude any influence of the metallic substrate. As shown previously, hydroxylation of MgO(001) requires the surface to be exposed to elevated pressures of water vapor, typically in the range of 10^{-4} mbar to 1 mbar [114]. The formation of a stable hydroxyl layer on MgO is suggested to proceed via hydrolysis of Mg-O surface bonds and leads to microscopic roughening of the MgO surface [115,116]. The results presented in this section were obtained from MgO thin film samples that were hydroxylated by exposure to 10^{-3} mbar D₂O at room temperature in a dedicated elevated pressure cell, which leads to a surface hydroxyl coverage of ~ 0.4 ML as estimated from quantitative XPS measurements [116].

A most obvious influence of hydroxyl groups on the properties of gold on the MgO surface is seen in Figure 27, which compares STM images of Au-MgO(001) (Figure 27a) and Au-MgO_{hydr} (Figure 27b) [117]. The first set of images was taken directly after Au deposition at room temperature (top), while the other set shows the surface state after subsequent heating to 600 K (bottom).

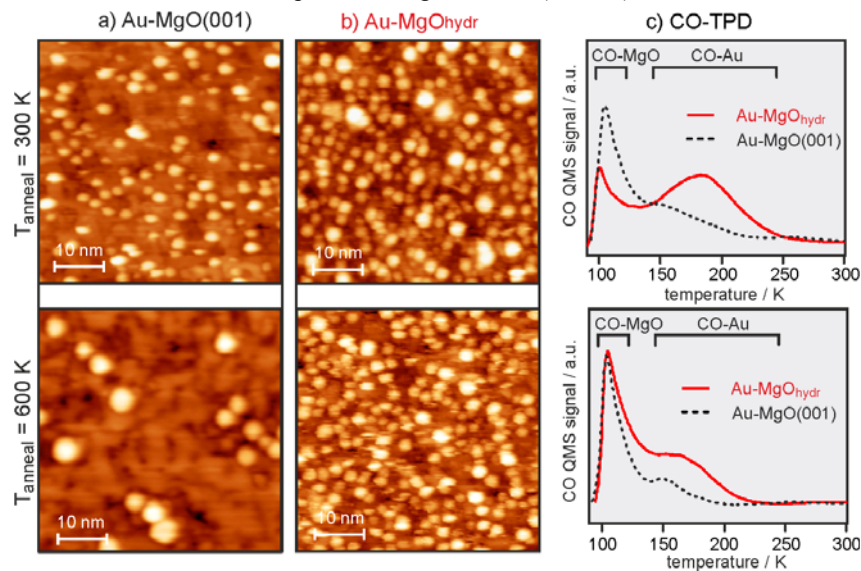


Figure 27: a) STM micrographs of 0.2 ML Au deposited on MgO(001) at room temperature taken immediately after Au deposition (top) and after subsequent heating to 600 K (bottom). b) Same as a) but for 0.02 ML Au deposited onto hydroxylated MgO (MgO_{hydr}). c) Comparison of CO-TPD spectra from 0.02 ML Au deposited on MgO(001) (black traces) and MgO_{hydr} (red traces) for Au particles grown at room temperature (top) and the same samples after heating to 600 K (bottom). CO was dosed at 100 K.

The Au particles are moderately dispersed over the MgO(001) surface at room temperature (Figure 27, top), but Ostwald ripening and particle coalescence lead to particle growth and a strong reduction of particle density after the elevated temperature treatment (Figure 27a, bottom), which is expected for this weakly interacting system. By contrast, the Au particle size and the particle density remain unaffected when the same thermal treatment is applied to Au- MgO_{hydr} (Figure 27b). The enhanced stability of Au- MgO_{hydr} towards sintering is also reflected in the CO adsorption capacity of the Au particles. The comparison of CO-TPD spectra from Au-MgO(001) and Au- MgO_{hydr} taken for particles grown at room temperature (Figure 27c, top) and after subsequent heating to 600 K (Figure 27c, bottom) clearly shows the enhancement of CO adsorption on Au- MgO_{hydr} , in line with the larger Au surface area of the more dispersed Au particles on MgO_{hydr} [118]. This is a significant finding in light of the importance of small Au particle size for the catalytic activity of oxide-supported Au catalysts. Indeed, chemical functionalization of a TiO_2 support with hydroxyls prior to the deposition of gold particles was found to have a strong enhancing effect on the CO oxidation activity [119].

What is the origin of the enhanced sinter resistance of Au particles on the hydroxylated MgO surface? As mentioned above, hydroxylation of MgO(001) is accompanied by microscopic roughening of the surface because of hydrolysis of Mg-O surface bonds. The morphological changes of the MgO surface may lead to increased barriers for Au atom diffusion and thus limited mobility, even at high temperature. On the other hand, additional or new nucleation centers may be created upon hydroxylation, which could enhance the adhesion of the Au particles because of a distinct chemical interaction with the substrate. While the first argument cannot be conclusively substantiated, direct evidence for the second one can be obtained with the help of spectroscopic methods.

Infrared spectroscopy using CO as a probe molecule has in the past been shown to provide valuable information about the charge state of gold particles [120]. While the stretching frequency of CO adsorbed on neutral Au particles is typically found in a narrow spectral region around 2100 cm^{-1} , the presence of positively (negatively) charged Au particles results in a shift to higher (lower) wavenumber as a result of reduced (increased) back-donation into the anti-bonding $2\pi^*$ orbital of CO has been discussed in the previous section. We noted that for CO adsorbed on neutral, single gold atoms on the MgO(001) surface, a $\nu(\text{CO})$ of 1852 cm^{-1} was observed as a result of internal charge reorganization in the MgO-Au-CO adsorption complex (see section 3 above, Figure 28a) [121]. This very particular characteristic represents an easily accessible spectroscopic indicator for the presence of single Au atoms on MgO and its presence or absence provides information about

the nucleation of Au on modified MgO surfaces, such as the hydroxylated one investigated here. Indeed, this signal cannot be recovered for gold deposited at 100 K onto MgO_{hydr} , which provides an initial evidence for the different nucleation of gold on this surface relative to clean $\text{MgO}(001)$. More specific information about the state of gold nucleated on MgO_{hydr} is obtained by looking into the spectral region around 2100 cm^{-1} , where CO vibrational signals from Au particles are expected. Two bands at 2165 cm^{-1} and 2125 cm^{-1} are observed, which are significantly blue-shifted relative to CO on neutral gold and are indicative for the presence of cationic or oxidized Au species on MgO_{hydr} [117]. The cationic nature of Au is also inferred from the corresponding XPS spectrum taken from this sample [117], which exhibits two Au $4f_{7/2}$ signals at 86.9 eV and 85.3 eV binding energy - significantly shifted to higher binding energy relative to bulk gold (84.0 eV).

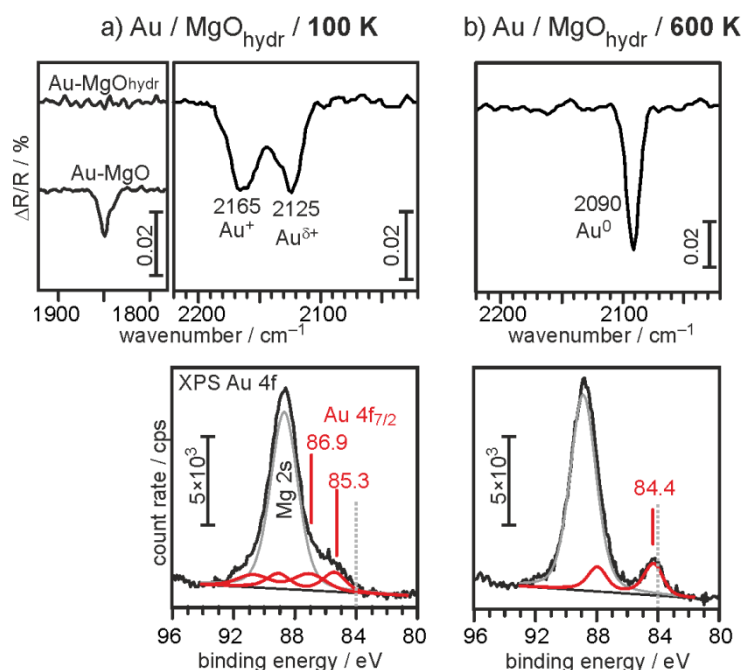


Figure 28: a) CO-IRAS spectra (top) and Au 4f XPS spectrum from 0.05 ML Au deposited at 100 K onto MgO_{hydr} . b) Same as a) taken after annealing of the samples to 600 K.

Since hydroxyl groups are obviously involved in the nucleation of Au on MgO_{hydr} , an impact of Au nucleation is also expected in the hydroxyl IR spectra. The top-most spectrum in Figure 29 displays the OD spectral detail of the infrared spectrum obtained from MgO_{hydr} for the specific hydroxylation conditions used in this experiment (10^{-3} mbar D_2O at room temperature for 180 sec.). The broad band can be deconvoluted into three signal components with $\nu(\text{OD}) = 2737, 2745$ and 2753

cm^{-1} , respectively, which are assigned to isolated and hydrogen-bond acceptor hydroxyls on the MgO surface (the corresponding OH bands are found at around 3750 cm^{-1}) [122]. Upon deposition of gold, the intensity of the OD signal at 2737 cm^{-1} is reduced (0.02 ML Au, Figure 28a, middle) and by increasing the Au coverage further, this signal is almost completely depleted (0.2 ML Au, Figure 28a, bottom). This result clearly indicates a very specific interaction of Au with hydroxylated MgO that involves only one particular surface hydroxyl site [117].

To obtain more detailed structural information about the specific hydroxyl site that is involved in the interaction with Au, it is instructive to inspect the OD-IR signals from MgO_{hydr} as obtained following hydroxylation of $\text{MgO}(001)$ at increasing D_2O partial pressure (Figure 28b). The series of IR spectra shows, from top to bottom, an increasing hydroxyl coverage, in agreement with the water-vapor pressure dependent hydroxylation activity of MgO, and corresponding shifts of the OD-IR frequencies, which indicate that different hydroxyl states (coordination, H-bonding) are populated as a function of hydroxyl coverage. Of particular importance for the present discussion is the fact that hydroxyl species exhibiting stretching frequencies of $2730\text{-}2740 \text{ cm}^{-1}$, i.e. in the range of the OD that is depleted upon deposition of gold (Figure 28a), appear exclusively after hydroxylation at low (10^{-4} mbar) water vapor pressure (Figure 28b). It can be expected that under these conditions the $\text{MgO}(001)$ terraces are not affected by water, and hydroxylation occurs exclusively by water dissociation at defect sites. From STM investigations it is clear that step sites are the most abundant defect sites on MgO thin films as used in the present study (Figure 28c). This leads us to propose that hydroxyl groups located at step sites such as the one sketched in Figure 29 are involved in the nucleation of gold on MgO_{hydr} [117].

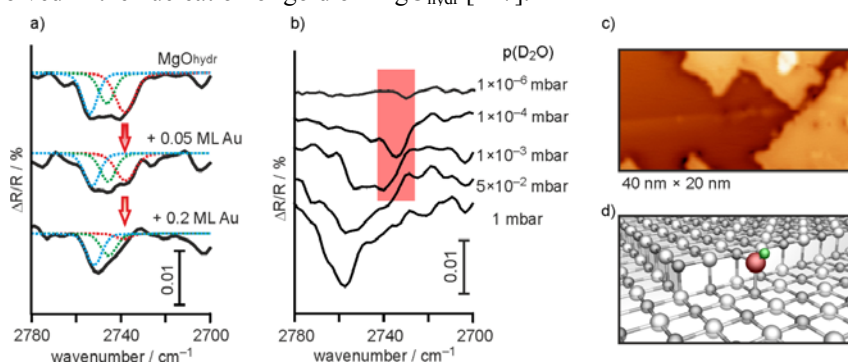


Figure 29: a) IRAS spectra showing the OD spectral detail of MgO_{hydr} (top), and after subsequent deposition 0.02 ML and 0.2 ML Au. b) IRAS spectra showing the OD spectral detail of MgO_{hydr} after hydroxylation in water vapor at various pressures. c) STM micrograph of the surface of a $\text{MgO}(001)$ thin film grown on $\text{Ag}(001)$. d) Model of a di-coordinated OH group located on a step site, which is proposed to be the initial nucleation site of Au on MgO_{hydr} .

In summary, the STM, XPS and IRAS results presented in Figure 27-29 provide evidence for a selective chemical interaction between Au and hydroxyl groups on MgO. Hydroxyl groups were found to act as strong anchoring sites for Au and the spectroscopic results indicate that oxidized Au species are formed on MgO_{hydr} . The enhanced sinter stability of Au on MgO_{hydr} may consequently be explained by the stronger interaction of Au with the MgO surface due to the formation of strong Au-O interfacial bonds. Though Au-oxide species are not stable at elevated temperature and decompose (see Figure 28c, which shows that after 600 K annealing the Au particles are essentially neutral), this strong interfacial interaction is the main reason for the sinter resistance of Au on MgO_{hydr} .

4.2 Surface science approach to supported Au catalyst preparation.

The results presented in the previous section have shown that chemical modification of an oxide surface with hydroxyl groups can have a strong stabilizing effect on Au particles, which is an important criterion in Au-related catalysis. The strong impact of Au particle size on the catalytic activity of oxide-supported Au as demonstrated by Haruta [113] were synthesized by co-precipitation from aqueous solutions containing HAuCl_4 and the nitrate of transition metals such as Fe, Co, or Ni. This type of preparation has later on been replaced by another procedure, which consists of suspending a metal oxide (the support) in a HAuCl_4 solution adjusted to a fixed pH in the range pH 7 – pH 10, aging of the solution for 1 hour at 343 K, followed by washing with distilled water, drying and calcination. This method is frequently termed deposition-precipitation (DP), although several conditions that are typical for DP, such as the gradual rise of pH and the preferential precipitation of the precursor at the interface, are not met as outlined by Louis et al [123]. A critical factor for obtaining small Au nanoparticles is the removal of chlorine from the supported phase, as chlorine enhances the mobility of Au species during drying and calcination. This is achieved by replacement of the Cl ligands in AuCl_4^- ions by hydroxo ligands through hydrolysis at neutral or alkaline pH such that Au-hydroxo complexes ($\text{Au}(\text{OH})_4^-$ or $\text{AuCl}(\text{OH})_3^-$) primary precursors interacting with the support, and by the washing step, which eliminates chlorine from the support surface.

The DP approach used for the preparation of supported Au catalysts is particularly well suited for studying the deposition of Au onto single-crystalline oxide supports from an Au precursor solution because it merely requires the oxide surface to be contacted with the precursor solution and does not rely on the presence of pores such as in incipient wetness impregnation, or the simultaneous precipitation of the support and the active metallic phase as done in coprecipitation. We attempted to recreate a situation similar to a DP procedure reported by Haruta by exposing the surface of a 10 nm thin $\text{Fe}_3\text{O}_4(111)$ film grown on Pt(111) to an aqueous solution of HAuCl_4 adjusted to pH 10. $\text{Fe}_3\text{O}_4(111)/\text{Pt}(111)$ was chosen

because of its high stability in aqueous solutions, as previously shown in our studies of Pd deposition from both strongly acidic [124] and strongly alkaline precursor solutions [125], as well as because of its conducting properties, which allows STM to be straightforwardly applied for morphological characterization.

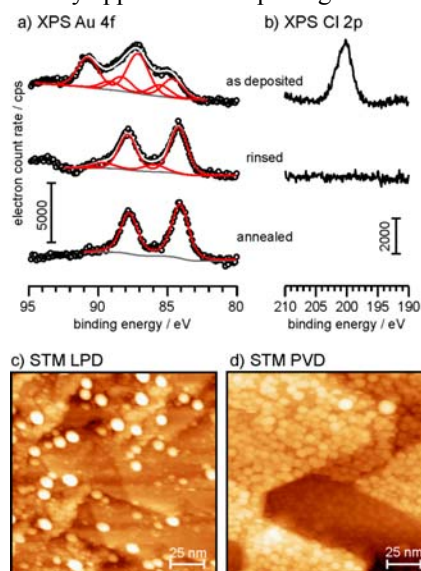


Figure 30: Au 4f (a) and Cl 2p (b) photoemission spectra from an Au-Fe₃O₄(111) sample at different stages of preparation (from top to bottom: "as deposited" is after drying; "rinsed" is after rinsing with distilled water; "annealed" is after additional heating to 600 K in UHV). c) STM image (150 nm x 150 nm) of the annealed Au-Fe₃O₄(111) sample prepared via aqueous Au precursor. d) STM image (150 nm x 150 nm) of an annealed Au-Fe₃O₄(111) sample prepared by physical vapor deposition of Au in UHV.

Figure 30a and Figure 30b display the Au 4f and Cl 2p photoemission spectra from an Au-Fe₃O₄(111) sample obtained by exposure of Fe₃O₄(111) to 1 mM HAuCl₄, pH10, for 5 min. at room temperature, after individual stages of preparation. The "as deposited" state represents the raw catalyst, which has been dried at room temperature but not rinsed. The main Au component present at this stage of preparation exhibits an Au 4f_{7/2} binding energy of 87.1 eV, which is in line with values reported for strongly oxidized Au and Au(OH)₃. The hydroxo complex [Au(OH)₄]⁻ is the main hydrolysis product of aqueous HAuCl₄ at pH 10 and the occurrence of the high binding energy Au 4f component in XPS strongly supports previous conclusions about the Au-hydroxo complex as the main adsorbing species during DP of Au. In addition, two Au 4f_{7/2} components at lower binding energy, at 85.5 eV and 84.6 eV, are present, which are attributed to oxidic and metallic Au resulting from partial decomposition of the Au-hydroxo precursor on the surface. As expected, a large amount of chloride is present on the raw catalyst.

Rinsing the surface with distilled water completely removed chloride from the surface, but led in addition to reduction of the Au precursor to metallic Au, which exhibits an Au $4f_{7/2}$ binding energy of 84.2 eV at this stage of preparation (Figure 3.3a and Figure 3.3b, “rinsed”). Subsequent heating to 600 K in UHV leads only to a small additional 0.1 eV shift of the Au $4f_{7/2}$ component to 84.1 eV (Figure 30a, “annealed”).

The XPS results provide already a good indication for the successful realization of Au deposition onto the $\text{Fe}_3\text{O}_4(111)$ surface from aqueous precursors. In order to obtain further proof, the annealed Au- $\text{Fe}_3\text{O}_4(111)$ model catalyst was investigated by STM. Figure 30c displays a corresponding image taken in air, wherein the bright features are assigned to Au nanoparticles. Closer inspection of this image reveals a bimodal particle size distribution, with the larger particles exhibiting a diameter of 6-8 nm, and some smaller ones, which are more abundant on the left side of the STM image, with a diameter of about 4 nm. For comparison, Figure 30d shows an STM image of a $\text{Fe}_3\text{O}_4(111)$ surface with Au particles obtained by physical vapor deposition of Au in UHV followed by annealing to 600 K. In this case, the Au particles are homogeneously distributed over the entire surface and the particle size distribution is narrow.

The chemical complexity of the system as well as the different interaction of Au with the chemically modified substrate is most probably responsible for the more heterogeneous Au particle distribution and morphology on the Au- $\text{Fe}_3\text{O}_4(111)$ sample prepared via the DP approach as compared the sample prepared in UHV. While more work is certainly necessary to understand the details of the metal-support interaction in this particular case, this work has demonstrated that progress is being made in applying surface science methodologies to study Au catalyst preparation procedures.

5 Synopsis

The growth of Au on ultrathin films and thicker, more bulk-like substrates by physical vapor deposition has been thoroughly studied and analyzed. The combination of imaging and spectroscopic techniques has allowed us derive a detailed picture of how clusters form from single Au atoms to clusters and further on to nano particles. The influence of charge of the particles has been discussed and their relation to the adsorption of CO molecules. By comparing three case studies, i.e. MgO, alumina and ironoxide, the influence of the nature of the support, in particular with respect to the charge has been elucidated. While ultrathin MgO and alumina lead to electron transfer to the supported Au, ironoxide leads to transfer from the Au to the support. In order to proceed to more realistic supports we have modified the magnesia support chemically by hydroxylation and discuss the consequences for Au particle formation, as well as the impact of this modification on the particle charge. In the case of an ironoxide support it has even been possible to

study Au particle deposition from solution and it is found that if certain conditions for reduction and calcination are used the result is rather similar to a preparation of Au particles from physical vapor deposition. This study also shows that Michael Mingos comments on the comparability of molecular compounds and surface adsorbates have been close to the truth.

References

- [1] Mingos DMP (1984) Polyhedral skeletal electron pair approach. *Acc Chem Res* 17 (9):311-319. doi:10.1021/ar00105a003
- [2] Mingos DMP (1984) Gold cluster compounds. *Gold Bull* 17 (1):5-12. doi:10.1007/BF03214670
- [3] Wade K (1971) The structural significance of the number of skeletal bonding electron-pairs in carboranes, the higher boranes and borane anions, and various transition-metal carbonyl cluster compounds. *J Chem Soc D* 0 (15):792-793. doi:10.1039/C29710000792
- [4] Gillespie RJ, Hargittai I (1991) *The VSEPR Model of Molecular Geometry*. 8. edn. Allyn & Bacon, Boston
- [5] Ertl G (2007) *Reactions At Surfaces: From Atoms To Complexity*. http://www.nobelprize.org/nobel_prizes/chemistry/laureates/2007/ertl_lecture.pdf.
- [6] Schauer mann S, Nilius N, Shaikhutdinov S, Freund H-J (2012) Nanoparticles for Heterogeneous Catalysis: New Mechanistic Insights. *Acc Chem Res*. doi:10.1021/ar300225s
- [7] Pacchioni G, Freund H (2012) Electron Transfer at Oxide Surfaces. The MgO Paradigm: from Defects to Ultrathin Films. *Chem Rev* 113 (6):4035-4072. doi:10.1021/cr3002017
- [8] Risse T, Shaikhutdinov S, Nilius N, Sterrer M, Freund H-J (2008) Gold Supported on Thin Oxide Films: From Single Atoms to Nanoparticles. *Acc Chem Res* 41 (8):949-956
- [9] Freund HJ (2010) Model Studies in Heterogeneous Catalysis. *Chem Eur J* 16 (31):9384-9397. doi:10.1002/chem.201001724
- [10] Haruta M (2002) Catalysis of gold nanoparticles deposited on metal oxides. *CatTech* 6 (3):102-115
- [11] Haruta M, Tsubota S, Kobayashi T, Kageyama H, Genet MJ, Delmon B (1993) Low-Temperature Oxidation of CO over Gold Supported on TiO₂, α -Fe₂O₃, and Co₃O₄. *J Catal* 144 (1):175-192. doi:10.1006/jcat.1993.1322
- [12] Winkelmann F, Wohlrab S, Libuda J, Bäumer M, Cappus D, Menges M, Al-Shamery K, Kuhlenbeck H, Freund HJ (1994) Adsorption on oxide surfaces: structure and dynamics. *Surf Sci* 307-309 (Part 2):1148
- [13] Wichtendahl R, Rodriguez-Rodrigo M, Härtel U, Kuhlenbeck H, Freund H-J (1999) TDS study of the bonding of CO and NO to vacuum-cleaved NiO(100). *Surf Sci* 423 (1):90-98
- [14] Wichtendahl R, Rodriguez-Rodrigo M, Härtel U, Kuhlenbeck H, Freund HJ (1999) Thermodesorption of CO and NO from vacuum-cleaved NiO(100) and MgO(100). *Phys Status Solidi A* 173 (1):93-100. doi:10.1002/(sici)1521-396x(199905)173:1<93::aid-pssa93>3.0.co;2-4

- [15] Sterrer M, Risse T, Heyde M, Rust H-P, Freund H-J (2007) Crossover from Three-Dimensional to Two-Dimensional Geometries of Au Nanostructures on Thin MgO(001) Films: A Confirmation of Theoretical Predictions. *Phys Rev Lett* 98 (20):206103
- [16] Yulikov M, Sterrer M, Heyde M, Rust HP, Risse T, Freund H-J, Pacchioni G, Scagnelli A (2006) Binding of Single Gold Atoms on Thin MgO(001) Films. *Phys Rev Lett* 96 (14):146804
- [17] Nambu A, Graciani J, Rodriguez JA, Wu Q, Fujita E, Sanz JF (2006) N doping of TiO₂(110): Photoemission and density-functional studies. *J Chem Phys* 125 (9):094706
- [18] Rodriguez JA, Hanson JC, Kim J-Y, Liu G, Iglesias-Juez A, Fernández-García M (2003) Properties of CeO₂ and Ce_{1-x}ZrxO₂ Nanoparticles: X-ray Absorption Near-Edge Spectroscopy, Density Functional, and Time-Resolved X-ray Diffraction Studies. *J Phys Chem B* 107 (15):3535-3543. doi:10.1021/jp022323i
- [19] Xu Y, Li J, Zhang Y, Chen W (2003) CO adsorption on MgO(001) surface with oxygen vacancy and its low-coordinated surface sites: embedded cluster model density functional study employing charge self-consistent technique. *Surf Sci* 525 (1-3):13-23. doi:10.1016/s0039-6028(02)02566-9
- [20] Neyman KM, Ruzankin SP, Rösch N (1995) Adsorption of CO molecules on a MgO(001) surface. Model cluster density functional study employing a gradient-corrected potential. *Chem Phys Lett* 246 (6):546-554. doi:[http://dx.doi.org/10.1016/0009-2614\(95\)01150-X](http://dx.doi.org/10.1016/0009-2614(95)01150-X)
- [21] Neyman KM, Roesch N (1992) Co Bonding and Vibrational-Modes on a Perfect MgO(001) Surface - Lcgto-Ldf Model Cluster Investigation. *Chem Phys* 168 (2-3):267-280
- [22] Pacchioni G (2000) Ab initio theory of point defects in oxide materials: structure, properties, chemical reactivity. *Solid State Sci* 2 (2):161-179. doi:10.1016/s1293-2558(00)00113-8
- [23] Del Vitto A, Pacchioni G, Delbecq F, Sautet P (2005) Au Atoms and Dimers on the MgO(100) Surface: A DFT Study of Nucleation at Defects *J Phys Chem B* 109 (16):8040-8048
- [24] Street SC, Xu C, Goodman DW (1997) THE PHYSICAL AND CHEMICAL PROPERTIES OF ULTRATHIN OXIDE FILMS. *Annu Rev Phys Chem* 48 (1):43-68. doi:doi:10.1146/annurev.physchem.48.1.43
- [25] Chambers SA (2000) Epitaxial growth and properties of thin film oxides. *Surf Sci Rep* 39 (5):105-180
- [26] Bäumer M, Freund HJ (1999) Metal deposits on well-ordered oxide films. *Progr Surf Sci* 61 (7-8):127-198. doi:10.1016/s0079-6816(99)00012-x
- [27] Giordano L, Cinquini F, Pacchioni G (2006) Tuning the surface metal work function by deposition of ultrathin oxide films: Density functional calculations. *Phys Rev B* 73 (4):045414
- [28] Pacchioni G, Giordano L, Baistrocchi M (2005) Charging of Metal Atoms on Ultrathin MgO/Mo(100) Films. *Phys Rev Lett* 94 (22):226104
- [29] Bonzel HP (1988) Alkali-Metal-Affected Adsorption of Molecules on Metal-Surfaces. *Surf Sci Rep* 8 (2):43-125
- [30] Diehl RD, McGrath R (1996) Structural studies of alkali metal adsorption and coadsorption on metal surfaces. *Surf Sci Rep* 23 (2-5):43-171. doi:[http://dx.doi.org/10.1016/0167-5729\(95\)00010-0](http://dx.doi.org/10.1016/0167-5729(95)00010-0)
- [31] Kliewer J, Berndt R (2001) Low temperature scanning tunneling microscopy of Na on Cu(111). *Surf Sci* 477 (2-3):250-258. doi:[http://dx.doi.org/10.1016/S0039-6028\(01\)00891-3](http://dx.doi.org/10.1016/S0039-6028(01)00891-3)
- [32] Sterrer M, Risse T, Martinez Pozzoni U, Giordano L, Heyde M, Rust H-P, Pacchioni G, Freund H-J (2007) Control of the Charge State of Metal Atoms on Thin MgO Films. *Phys Rev Lett* 98 (9):096107

- [33] Sterrer M, Risse T, Giordano L, Heyde M, Nilius N, Rust HP, Pacchioni G, Freund H-J (2007) Palladium Monomers, Dimers, and Trimers on the MgO(001) Surface Viewed Individually *Angew Chem Int Ed* 46 (45):8703-8706
- [34] Wu SW, Ogawa N, Nazin GV, Ho W (2008) Conductance Hysteresis and Switching in a Single-Molecule Junction. *J Phys Chem C* 112 (14):5241-5244.
doi:10.1021/jp7114548
- [35] Wu SW, Nazin GV, Chen X, Qiu XH, Ho W (2004) Control of Relative Tunneling Rates in Single Molecule Bipolar Electron Transport. *Phys Rev Lett* 93 (23):236802
- [36] Jaeger RM, Kuhlenbeck H, Freund HJ, Wuttig M, Hoffmann W, Franchy R, Ibach H (1991) Formation of a well-ordered aluminium oxide overlayer by oxidation of NiAl(110). *Surf Sci* 259 (3):235-252. doi:10.1016/0039-6028(91)90555-7
- [37] Nilius N, Pirovano VG, Bradzova V, Kulawik M, Sauer J, Freund H-J (?). submitted
- [38] Giordano L, Pacchioni G (2011) Oxide Films at the Nanoscale: New Structures, New Functions, and New Materials. *Acc Chem Res* 44 (11):1244-1252.
doi:10.1021/ar200139y
- [39] Nilius N, Ganduglia-Pirovano MV, Brazdova V, Kulawik M, Sauer J, Freund HJ (2010) Electronic properties and charge state of gold monomers and chains adsorbed on alumina thin films on NiAl(110). *Phys Rev B* 81 (4):045422
- [40] Kulawik M, Nilius N, Freund HJ (2006) Influence of the Metal Substrate on the Adsorption Properties of Thin Oxide Layers: Au Atoms on a Thin Alumina Film on NiAl(110). *Phys Rev Lett* 96 (3):036103
- [41] Hamers RJ (1989) Atomic-Resolution Surface Spectroscopy with the Scanning Tunneling Microscope. *Annu Rev Phys Chem* 40 (1):531-559.
doi:doi:10.1146/annurev.pc.40.100189.002531
- [42] Tersoff J, Hamann DR (1983) Theory and Application for the Scanning Tunneling Microscope. *Phys Rev Lett* 50 (25):1998-2001
- [43] Kittel C (1996) *Introduction to Solid State Physics*. 7th edn. Wiley, New York
- [44] Schmid M, Shishkin M, Kresse G, Napetschnig E, Varga P, Kulawik M, Nilius N, Rust HP, Freund HJ (2006) Oxygen-Deficient Line Defects in an Ultrathin Aluminum Oxide Film. *Phys Rev Lett* 97 (4):046101-046101-046104
- [45] Rienks EDL, Nilius N, Rust HP, Freund HJ (2005) Surface Potential of a Polar Oxide Film: FeO on Pt(111). *Phys Rev B* 71:2414041-2414044
- [46] Giordano L, Pacchioni G, Goniakowski J, Nilius N, Rienks EDL, Freund H-J (2008) Charging of Metal Adatoms on Ultrathin Oxide Films: Au and Pd on FeO/Pt(111). *Phys Rev Lett* 101 (2):026102
- [47] Simic-Milosevic V, Heyde M, Nilius N, Koenig T, Rust HP, Sterrer M, Risse T, Freund HJ, Giordano L, Pacchioni G (2008) Au Dimers on Thin MgO(001) Films: Flat and Charged or Upright and Neutral? *J Am Chem Soc* 130 (25):7814-7815.
doi:10.1021/ja8024388
- [48] Simic-Milosevic V, Heyde M, Lin X, König T, Rust H-P, Sterrer M, Risse T, Nilius N, Freund H-J, Giordano L, Pacchioni G (2008) Charge-induced formation of linear Au clusters on thin MgO films: Scanning tunneling microscopy and density-functional theory study. *Phys Rev B* 78 (23):235429
- [49] Nilius N (2009) Properties of oxide thin films and their adsorption behavior studied by scanning tunneling microscopy and conductance spectroscopy. *Surf Sci Rep* 64 (12):595-659
- [50] Frondelius P, Häkkinen H, Honkala K (2007) Adsorption of small Au clusters on MgO and MgO/Mo: the role of oxygen vacancies and the Mo-support. *New J Phys* 9:339.
doi:<http://dx.doi.org/10.1088/1367-2630/9/9/339>
- [51] Nilius N, Wallis TM, Ho W (2002) Development of One-Dimensional Band Structure in Artificial Gold Chains *Science* 297:1853-1856

- [52] Wallis TM, Nilius N, Ho W (2002) Electronic Density Oscillations in Gold Atomic Chains Assembled Atom by Atom. *Phys Rev Lett* 89 (23):236802
- [53] Nilius N, Wallis TM, Persson M, Ho W (2003) Distance Dependence of the Interaction between Single Atoms: Gold Dimers on NiAl(110). *Phys Rev Lett* 90 (19):196103
- [54] Henry CR (1998) Surface studies of supported model catalysts. *Surf Sci Rep* 31:231-326
- [55] Ricci D, Bongiorno A, Pacchioni G, Landman U (2006) Bonding Trends and Dimensionality Crossover of Gold Nanoclusters on Metal-Supported MgO Thin Films. *Phys Rev Lett* 97 (3):036106
- [56] Lin X, Nilius N, Freund HJ, Walter M, Frondelius P, Honkala K, Häkkinen H (2009) Quantum Well States in Two-Dimensional Gold Clusters on MgO Thin Films. *Phys Rev Lett* 102 (20):206801-206804
- [57] Lin X, Nilius N, Sterrer M, Koskinen P, Häkkinen H, Freund H-J (2010) Characterizing low-coordinated atoms at the periphery of MgO-supported Au islands using scanning tunneling microscopy and electronic structure calculations. *Phys Rev B* 81 (15):153406-153401-153404
- [58] Andersin J, Nevalaita J, Honkala K, Häkkinen H (2013) The Redox Chemistry of Gold with High-Valence Doped Calcium Oxide. *Angew Chem Int Ed* 52 (5):1424-1427. doi:10.1002/anie.201208443
- [59] Walter M, Frondelius P, Honkala K, Häkkinen H (2007) Electronic Structure of MgO-Supported Au Clusters: Quantum Dots Probed by Scanning Tunneling Microscopy. *Phys Rev Lett* 99 (9):096102
- [60] de Heer WA (1993) The physics of simple metal clusters: experimental aspects and simple models. *Rev Mod Phys* 65 (3):611-676
- [61] Valden M, Lai X, Goodman DW (1998) Onset of Catalytic Activity of Gold Clusters on Titania with the Appearance of Nonmetallic Properties. *Science* 281 1647-1650
- [62] Cabrera N, Mott NF (1948) Theory of the oxidation of metals. *Rep Progr Phys* 12:163
- [63] Molina LM, Hammer B (2005) Some recent theoretical advances in the understanding of the catalytic activity of Au. *Appl Catal, A* 291 (1-2):21-31. doi:10.1016/j.apcata.2005.01.050
- [64] Green IX, Tang WJ, Neurock M, Yates JT (2011) Spectroscopic Observation of Dual Catalytic Sites During Oxidation of CO on a Au/TiO₂ Catalyst *Science* 333:736-739
- [65] Abbet S, Riedo E, Brune H, Heiz U, Ferrari AM, Giordano L, Pacchioni G (2001) Identification of Defect Sites on MgO(100) Thin Films by Decoration with Pd Atoms and Studying CO Adsorption Properties. *J Am Chem Soc* 123 (25):6172-6178
- [66] Lin X, Yang B, Benia HM, Myrach P, Yulikov M, Aumer A, Brown M, Sterrer M, Bondarchuk O, Kieseritzky E, Rocker J, Risse T, Gao H, Nilius N, Freund HJ (2010) Charge-Mediated Adsorption Behavior of CO on MgO-Supported Au Clusters. *J Am Chem Soc* 132 (22):7745-7749
- [67] Hashmi ASK, Hutchings GJ (2006) Gold Catalysis. *Angew Chem Int Ed* 45 (47):7896-7936. doi:10.1002/anie.200602454
- [68] Herzing AA, Kiely CJ, Carley AF, Landon P, Hutchings GJ (2008) Identification of Active Gold Nanoclusters on Iron Oxide Supports for CO Oxidation. *Science* 321:1331-1335. doi:10.1126/science.1159639
- [69] Chen MS, Goodman DW (2004) The Structure of Catalytically Active Au on Titania. *Science* 306:252-255
- [70] Ekardt W (ed) (1999) *Metal Clusters*. John Wiley, Chichester
- [71] Kreibig U, Vollmer W (eds) (1995) *Optical properties of metal clusters*, vol 25. Springer Series in Materials Science. Springer-Verlag, Berlin-New York

- [72] Wendt S, Sprunger PT, Lira E, Madsen GKH, Li Z, Hansen JØ, Matthiesen J, Blekinge-Rasmussen A, Lægsgaard E, Hammer B, Besenbacher F (2008) The Role of Interstitial Sites in the Ti3d Defect State in the Band Gap of Titania. *Science* 320 (5884):1755-1759. doi:10.1126/science.1159846
- [73] Kim HY, Lee HM, Pala RGS, Shapovalov V, Metiu H (2008) CO Oxidation by Rutile TiO₂(110) Doped with V, W, Cr, Mo, and Mn. *J Phys Chem C* 112 (32):12398-12408. doi:10.1021/jp802296g
- [74] Shapovalov V, Metiu H (2007) Catalysis by doped oxides: CO oxidation by AuxCe_{1-x}O₂. *J Catal* 245 (1):205-214. doi:<http://dx.doi.org/10.1016/j.jcat.2006.10.009>
- [75] Mammen N, Narasimhan S, Gironcoli Sd (2011) Tuning the Morphology of Gold Clusters by Substrate Doping. *J Amer Chem Soc* 133 (9):2801-2803. doi:10.1021/ja109663g
- [76] Wang JX, Lunsford JH (1986) Characterization of [Li+O] centers in lithium-doped magnesium oxide catalysts. *J Phys Chem* 90 (22):5883-5887. doi:10.1021/j100280a084
- [77] Ito T, Wang J, Lin CH, Lunsford JH (1985) Oxidative dimerization of methane over a lithium-promoted magnesium oxide catalyst. *J Am Chem Soc* 107 (18):5062-5068. doi:10.1021/ja00304a008
- [78] Pala RGS, Metiu H (2007) The Structure and Energy of Oxygen Vacancy Formation in Clean and Doped, Very Thin Films of ZnO. *J Phys Chem C* 111 (34):12715-12722. doi:10.1021/jp073424p
- [79] Nolan M, Verdugo VS, Metiu H (2008) Vacancy formation and CO adsorption on gold-doped ceria surfaces. *Surf Sci* 602 (16):2734-2742. doi:10.1016/j.susc.2008.06.028
- [80] Shao X, Prada S, Giordano L, Pacchioni G, Nilius N, Freund H-J (2011) Tailoring the Shape of Metal Ad-Particles by Doping the Oxide Support. *Angew Chem Int Ed* 50 (48):11525-11527. doi:10.1002/anie.201105355
- [81] Stavale F, Shao X, Nilius N, Freund H-J, Prada S, Giordano L, Pacchioni G (2012) Donor Characteristics of Transition-Metal-Doped Oxides: Cr-Doped MgO versus Mo-Doped CaO. *J Am Chem Soc* 134 (28):11380-11383. doi:10.1021/ja304497n
- [82] Stavale F, Nilius N, Freund H-J (2012) Cathodoluminescence of near-surface centres in Cr-doped MgO(001) thin films probed by scanning tunnelling microscopy *New J Phys* 14:033006. doi:<http://iopscience.iop.org/1367-2630/14/3/033006/>
- [83] Prada S, Giordano L, Pacchioni G (2013) Charging of Gold Atoms on Doped MgO and CaO: Identifying the Key Parameters by DFT Calculations. *J Phys Chem C* 117 (19):9943-9951. doi:10.1021/jp401983m
- [84] Henderson B, Imbusch GF (eds) (1989) *Optical Spectroscopy of Inorganic Solids*. Oxford University Press, Oxford
- [85] Lide DR (1996) *CRC Handbook of Chemistry and Physics*. CRC Press,
- [86] Benia HM, Myrach P, Gonchar A, Risse T, Nilius M, Freund HJ (2010) Electron trapping in misfit dislocations of MgO thin films. *Phys Rev B* 81:241415. doi:<http://link.aps.org/doi/10.1103/PhysRevB.81.241415>
- [87] Li B, Metiu H (2010) DFT Studies of Oxygen Vacancies on Undoped and Doped La₂O₃ Surfaces. *J Phys Chem C* 114 (28):12234-12244. doi:10.1021/jp103604b
- [88] Hu Z, Li B, Sun X, Metiu H (2011) Chemistry of Doped Oxides: The Activation of Surface Oxygen and the Chemical Compensation Effect. *J Phys Chem C* 115 (7):3065-3074. doi:10.1021/jp110333z
- [89] Shao X, Nilius N, Freund H-J (2012) Li/Mo Codoping of CaO Films: A Means to Tailor the Equilibrium Shape of Au Deposits. *J Am Chem Soc* 134 (5):2532-2534. doi:10.1021/ja211396t
- [90] Sterrer M, Heyde M, Novicki M, Nilius N, Risse T, Rust HP, Pacchioni G, Freund HJ (2006) Identification of color centers on MgO(001) thin films with scanning tunneling microscopy. *J Phys Chem B* 110 (1):46-49. doi:10.1021/jp056306f

- [91] Myrach P, Nilius N, Levchenko SV, Gonchar A, Risse T, Dinse K-P, Boatner LA, Frandsen W, Horn R, Freund H-J, Schlögl R, Scheffler M (2010) Temperature-Dependent Morphology, Magnetic and Optical Properties of Li-Doped MgO. *ChemCatChem* 2 (7):854-862. doi:10.1002/cctc.201000083
- [92] Mihaylov M, Knözinger H, Hadjiivanov K, Gates BC (2007) Characterization of the Oxidation States of Supported Gold Species by IR Spectroscopy of Adsorbed CO. *Chem Ing Tech* 79 (6):795-806. doi:10.1002/cite.200700029
- [93] Sterrer M, Yulikov M, Risse T, Freund H-J, Carrasco J, Illas F, Di Valentin C, Giordano L, Pacchioni G (2006) When the Reporter Induces the Effect: Unusual IR spectra of CO on Au1/MgO(001)/Mo(001). *Angew Chem Int Ed* 45 (16):2633-2635. doi:10.1002/anie.200504473
- [94] Oberholzer S, Bieri E, Schönenberger C, Giovannini M, Faist J (2006) Positive Cross Correlations in a Normal-Conducting Fermionic Beam Splitter. *Phys Rev Lett* 96 (4):046804
- [95] Yang B, Lin X, Gao H-J, Nilius N, Freund H-J (2010) CO Adsorption on Thin MgO Films and Single Au Adatoms: A Scanning Tunneling Microscopy Study. *J Phys Chem C* 114 (19):8997-9001. doi:10.1021/jp100757y
- [96] Ho W (2002) Single-molecule chemistry. *J Chem Phys* 117 (24):11033-11061
- [97] Lauhon LJ, Ho W (1999) Single-molecule vibrational spectroscopy and microscopy: CO on Cu(001) and Cu(110). *Phys Rev B* 60 (12):R8525-R8528
- [98] Nilius N, Wallis TM, Ho W (2002) Vibrational spectroscopy and imaging of single molecules: Bonding of CO to single palladium atoms on NiAl(110). *J Chem Phys* 117 (24):10947-10952
- [99] Wang H, Tobin RG, Lambert DK (1994) Coadsorption of hydrogen and CO on Pt(335): Structure and vibrational Stark effect. *J Chem Phys* 101 (5):4277-4287
- [100] Hammer B (2006) Special Sites at Noble and Late Transition Metal Catalysts. *Top Catal* 37 (1):3-16. doi:10.1007/s11244-006-0004-y
- [101] Sicolo S, Giordano L, Pacchioni G (2009) CO Adsorption on One-, Two-, and Three-Dimensional Au Clusters Supported on MgO/Ag(001) Ultrathin Films. *J Phys Chem C* 113 (23):10256-10263. doi:10.1021/jp9023266
- [102] Blyholder G (1964) Molecular Orbital View of Chemisorbed Carbon Monoxide. *J Phys Chem* 68:2772-2778
- [103] Hövel H, Barke I (2003) Large noble metal clusters: electron confinement and band structure effects. *New J Phys* 5 (1):31
- [104] Benia HM, Lin X, Gao HJ, Nilius N, Freund H-J (2007) Nucleation and Growth of Gold on MgO Thin Films: A Combined STM and Luminescence Study. *J Phys Chem C* 111 (28):10528-10533
- [105] Fielicke A, von Helden G, Meijer G, Simard B, Rayner DM (2005) Gold Cluster Carbonyls: Vibrational Spectroscopy of the Anions and the Effects of Cluster Size, Charge, and Coverage on the CO Stretching Frequency. *J Phys Chem B* 109 (50):23935-23940
- [106] Shaikhutdinov SK, Meyer R, Naschitzki M, Bäumer M, Freund HJ (2003) Size and Support Effects for CO Adsorption on Gold Model Catalysts. *Catalysis Letters* 86 (4):211-219. doi:10.1023/a:1022616102162
- [107] Ruggiero C, Hollins P (1997) Interaction of CO molecules with the Au(332) surface. *Surface Science* 377-379 (0):583-586. doi:[http://dx.doi.org/10.1016/S0039-6028\(96\)01451-3](http://dx.doi.org/10.1016/S0039-6028(96)01451-3)
- [108] Weststrate CJ, Lundgren E, Andersen JN, Rienks EDL, Gluhoi AC, Bakker JW, Groot IMN, Nieuwenhuys BE (2009) CO adsorption on Au(310) and Au(321): 6-Fold coordinated gold atoms. *Surface Science* 603 (13):2152-2157. doi:<http://dx.doi.org/10.1016/j.susc.2009.04.026>

- [109] Lemire C, Meyer R, Shaikhutdinov SK, Freund HJ (2004) CO adsorption on oxide supported gold: from small clusters to monolayer islands and three-dimensional nanoparticles. *Surface Science* 552 (1–3):27-34. doi:<http://dx.doi.org/10.1016/j.susc.2004.01.029>
- [110] Nilius N, Rienks EDL, Rust H-P, Freund H-J (2005) Self-Organization of Gold Atoms on a Polar FeO(111) Surface. *Phys Rev Lett* 95 (6):066101
- [111] Meyer R, Lemire C, Shaikhutdinov SK, Freund HJ (2004) Surface chemistry of catalysis by gold. *Gold Bull* 37 (1-2):72-124. doi:10.1007/bf03215519
- [112] Starr DE, Pazhetnov EM, Stadnichenko AI, Boronin AI, Shaikhutdinov SK (2006) Carbon films grown on Pt(111) as supports for model gold catalysts. *Surface Science* 600 (13):2688-2695. doi:<http://dx.doi.org/10.1016/j.susc.2006.04.035>
- [113] Haruta M, Kobayashi T, Sano H, Yamada N (1987) NOVEL GOLD CATALYSTS FOR THE OXIDATION OF CARBON-MONOXIDE AT A TEMPERATURE FAR BELOW 0-DEGREES-C. *Chemistry Letters* (2):405-408. doi:10.1246/cl.1987.405
- [114] Liu P, Kendelewicz T, Gordon GE, Parks GA (1998) Reaction of water with MgO(100) surfaces. Part I: Synchrotron X-ray photoemission studies of low-defect surfaces. *Surface Science* 412-13:287-314. doi:10.1016/s0039-6028(98)00444-0
- [115] Mejias JA, Berry AJ, Refson K, Fraser DG (1999) The kinetics and mechanism of MgO dissolution. *Chem Phys Lett* 314 (5-6):558-563. doi:10.1016/s0009-2614(99)00909-4
- [116] Carrasco E, Brown MA, Sterrer M, Freund HJ, Kwapien K, Sierka M, Sauer J (2010) Thickness-Dependent Hydroxylation of MgO(001) Thin Films. *Journal of Physical Chemistry C* 114 (42):18207-18214. doi:10.1021/jp105294e
- [117] Brown MA, Fujimori Y, Ringleb F, Shao X, Stavale F, Nilius N, Sterrer M, Freund HJ (2011) Oxidation of Au by Surface OH: Nucleation and Electronic Structure of Gold on Hydroxylated MgO(001). *Journal of the American Chemical Society* 133 (27):10668-10676. doi:10.1021/ja204798z
- [118] Brown MA, Carrasco E, Sterrer M, Freund HJ (2010) Enhanced Stability of Gold Clusters Supported on Hydroxylated MgO(001) Surfaces. *Journal of the American Chemical Society* 132 (12):4064-4065. doi:10.1021/ja100343m
- [119] Veith GM, Lupini AR, Dudney NJ (2009) Role of pH in the Formation of Structurally Stable and Catalytically Active TiO₂-Supported Gold Catalysts. *Journal of Physical Chemistry C* 113 (1):269-280. doi:10.1021/jp808249f
- [120] Mihaylov M, Knözinger H, Hadjiivanov K, Gates BC (2007) Characterization of the oxidation states of supported gold species by IR spectroscopy of adsorbed CO. *Chem Ing Tech* 79 (6):795-806. doi:10.1002/cite.200700029
- [121] Sterrer M, Yulikov M, Risse T, Freund HJ, Carrasco J, Illas F, Di Valentin C, Giordano L, Pacchioni G (2006) When the reporter induces the effect: Unusual IR spectra of CO on Au-1/MgO(001)/Mo(001). *Angew Chem Int Ed* 45 (16):2633-2635. doi:10.1002/anie.200504473
- [122] Chizallet C, Costentin G, Che M, Delbecq F, Sautet P (2007) Infrared characterization of hydroxyl groups on MgO: A periodic and cluster density functional theory study. *Journal of the American Chemical Society* 129 (20):6442-6452. doi:10.1021/ja068720e
- [123] Zanella R, Delannoy L, Louis C (2005) Mechanism of deposition of gold precursors onto TiO₂ during the preparation by cation adsorption and deposition-precipitation with NaOH and urea. *Appl Catal, A* 291 (1-2):62-72. doi:10.1016/j.apcata.2005.02.045
- [124] Wang HF, Ariga H, Dowler R, Sterrer M, Freund HJ (2012) Surface science approach to catalyst preparation - Pd deposition onto thin Fe₃O₄(111) films from PdCl₂ precursor. *Journal of Catalysis* 286:1-5. doi:10.1016/j.jcat.2011.09.026

- [125] Wang HF, Kaden WE, Dowler R, Sterrer M, Freund HJ (2012) Model oxide-supported metal catalysts - comparison of ultrahigh vacuum and solution based preparation of Pd nanoparticles on a single-crystalline oxide substrate. *Physical Chemistry Chemical Physics* 14 (32):11525-11533. doi:10.1039/c2cp41459g